

Numerical Characterization of Ultrasound Elastography for the Early
Detection of Deep Tissue Injuries

by

Kenton David Hamaluik

A thesis submitted in partial fulfillment of the requirements for the degree of

Master of Science

Department of Mechanical Engineering
University of Alberta

© Kenton Hamaluik, 2014

Abstract

Abstract goes here...

Preface

Chapter 3 of this thesis has been submitted for publication as K.D. Hamaluik, W. Moussa, M. Ferguson-Pell, “Numerical Characterization of Quasi-Static Ultrasound Elastography,” *IEEE Transactions on Medical Imaging* and is currently undergoing peer review. I was responsible for the study design, data collection, and manuscript composition. W. Moussa and M. Ferguson-Pell were the supervisory authors and assisted with manuscript composition.

Dedication

Lorem ipsum dolor sit amet, consectetuer adipiscing elit. Ut purus elit, vestibulum ut, placerat ac, adipiscing vitae, felis. Curabitur dictum gravida mauris. Nam arcu libero, nonummy eget, consectetuer id, vulputate a, magna. Donec vehicula augue eu neque. Pellentesque habitant morbi tristique senectus et netus et malesuada fames ac turpis egestas. Mauris ut leo. Cras viverra metus rhoncus sem. Nulla et lectus vestibulum urna fringilla ultrices. Phasellus eu tellus sit amet tortor gravida placerat. Integer sapien est, iaculis in, pretium quis, viverra ac, nunc. Praesent eget sem vel leo ultrices bibendum. Aenean faucibus. Morbi dolor nulla, malesuada eu, pulvinar at, mollis ac, nulla. Curabitur auctor semper nulla. Donec varius orci eget risus. Duis nibh mi, congue eu, accumsan eleifend, sagittis quis, diam. Duis eget orci sit amet orci dignissim rutrum.

Acknowledgements

Lorem ipsum dolor sit amet, consectetuer adipiscing elit. Ut purus elit, vestibulum ut, placerat ac, adipiscing vitae, felis. Curabitur dictum gravida mauris. Nam arcu libero, nonummy eget, consectetuer id, vulputate a, magna. Donec vehicula augue eu neque. Pellentesque habitant morbi tristique senectus et netus et malesuada fames ac turpis egestas. Mauris ut leo. Cras viverra metus rhoncus sem. Nulla et lectus vestibulum urna fringilla ultrices. Phasellus eu tellus sit amet tortor gravida placerat. Integer sapien est, iaculis in, pretium quis, viverra ac, nunc. Praesent eget sem vel leo ultrices bibendum. Aenean faucibus. Morbi dolor nulla, malesuada eu, pulvinar at, mollis ac, nulla. Curabitur auctor semper nulla. Donec varius orci eget risus. Duis nibh mi, congue eu, accumsan eleifend, sagittis quis, diam. Duis eget orci sit amet orci dignissim rutrum.

Table of Contents

1	Introduction	1
1.1	Motivation	1
1.2	Objective	3
1.3	Methodology	3
1.4	Thesis Outline	4
2	Literature Review	6
2.1	Deep Tissue Injuries	6
2.1.1	Aetiology and Histology	10
2.1.2	Detection	13
2.1.3	Prevention and Treatment	16
2.2	Ultrasound Elastography	17
2.2.1	Quasi-Static Ultrasound Elastography	18
2.2.2	Acoustic Radiation Force Impulse Imaging	18
2.2.3	Shear Wave Speed Quantification	18
2.3	Conclusion	18
3	Numerical Characterization of Quasi-Static Ultrasound Elastography	19
3.1	Introduction	19
3.2	Method	20
3.2.1	Formation of B-Mode Ultrasound Images	22
3.2.2	Finite-Element Model of Tissue Deformation Under Surface Distortion	23
3.2.3	Characterizing Quasi-Static Ultrasound Elastography .	25
3.2.4	Model Validation Using a Commercially Available Phantom	26
3.3	Results and Discussion	26

3.3.1	Finite Element Models of Ultrasound and Deformation	27
3.3.2	Resulting Elastograms	29
3.3.3	Numerical Characterizations	30
3.3.4	Physical Phantom Validation	45
3.4	Conclusion	47
4	Numerical Characterization of Acoustic Radiation Force Impulse Imaging	51
4.1	Introduction	51
4.2	Methods	51
4.2.1	Numerical Model	51
4.3	Results	52
5	Numerical Characterization of Shear Wave Speed Quantification	53
6	Conclusion	54
6.1	Clinical Need for DTI Detection	54
6.2	USE Provides Potential Diagnosis Capability	54
6.3	Future Work	54
6.3.1	Animal Studies?	54
6.3.2	Human Studies?	54
References		55
A	Source Code	77
A.1	Quasi-Static Ultrasound Elastography Simulations	77

List of Tables

3.1	Range of values of investigated parameters	21
3.2	CIRS Phantom Model Mechanical Properties	26

List of Figures

2.1	NPUAP pressure ulcer staging guidelines	8
2.2	Schematic representation of the time course of tissue stiffness changes in a deep tissue injury site.	12
3.1	Quasi-static model geometries	22
3.2	Point spread function used for simulating b-mode ultrasound scans	23
3.3	Sample deformation finite-element model results for a hard spherical lesion	28
3.4	Sample strain elastogram for a hard spherical lesion	30
3.5	Detection ability as it is related to true lesion stiffness ratio . .	31
3.6	Error characterization for a hard spherical lesion	32
3.7	Error characterization for: co-located, blurred boundary, clustered, and visible human lesion models	33
3.8	Quasi-static lesion size characterization	34
3.9	Quasi-static lesion depth characterization	35
3.10	Quasi-static lesion altitude characterization	36
3.11	Quasi-static ultrasound probing frequency characterization .	37
3.12	Quasi-static applied strain characterization	38
3.13	Quasi-static lesion separation distance characterization	39
3.14	Sample elastogram for two co-located lesions	40
3.15	Quasi-static lesion blur radius characterization	41
3.16	Quasi-static lesion density characterization	42
3.17	Sample elastogram for a set of clustered lesions	43
3.18	Quasi-static clustered lesion radius characterization	44
3.19	Quasi-static Visible Human model lesion width characterization	45
3.20	Sample elastogram of a Visible Human model lesion	46

3.21 Quasi-static characterization of lesion depth in a Visible Human model	47
3.22 Experimental validation of quasi-static model results	48

Nomenclature

Mathematical Symbols^{c1}

Abbreviation	Meaning
b_r	Blurred lesion blur radius
b_ρ	Clustered lesion density
d	Lesion depth
d	Visible Human lesion depth
δ_{sep}	Co-located lesion separation distance
E_{rel}	Lesion stiffness ratio
E_{lesion}	Young's modulus of lesion
E_{tissue}	Young's modulus of tissue
ε_{app}	Transducer-applied strain
ε_{lesion}	Measured lesion strain
$\varepsilon_{rel,measured}$	Measured lesion strain ratio
$\varepsilon_{rel,true}$	True lesion strain ratio
ε_{tissue}	Measured tissue strain
F	Applied body forces
f	Ultrasound frequency
Γ	Boundary domain
h	Lesion altitude
λ	Ultrasound wavelength
μ	Mean value
∇	Del operator
r_{bl}	Clustered lesion radius
$\emptyset S$	Lesion diameter
$\emptyset S$	Visible Human lesion width

^{c1} KH: I'm going to have to clean up these symbols.. a lot get re-used for different purposes

Abbreviation	Meaning
σ	Stress tensor
σ	Standard deviation
$\sigma_{applied}$	Stress applied to tissue
u	Displacement
u_0	Initial displacement
w_{active}	Total width of active transducer elements

Abbreviations

Abbreviation	Meaning
ARFI	Acoustic radiation force impulse
DTI	Deep tissue injury
IES	Intermittent electrical stimulation
MRI	Magnetic resonance imaging
NPUAP	National Pressure Ulcer Advisory Panel
PU	Pressure ulcer
SCI	Spinal cord injury
USE	Ultrasound elastography

Chapter 1

Introduction

1.1 Motivation

Pressure ulcers are debilitating wounds often suffered by people with limited mobility such as those undergoing lengthy surgical procedures, the elderly, and those with spinal cord injuries (SCI) [1]—up to 80 % of people with SCI will develop a pressure ulcer in their lifetime [2]. Pressure ulcers are generally characterized by a deterioration of the skin leading to painful open wounds and while many pressure ulcers may be blamed on excess friction and moisture at the skin surface, many can start as “deep tissue injuries” (DTI) which start deep below the skin surface—most often at the bone-muscle interface [3]. DTI are generally thought to be formed due to some combination of excessive deformation and ischemia resulting from sustained loading on localized tissue [4]–[6]. As of the time of writing, there is no clinically feasible method of detecting deep tissue injuries until they begin to damage the skin—even the National Pressure Ulcer Advisory Panel’s description of them is largely based on their appearance after the fact [7]. With our inability to detect these forming injuries and subsequently implement deep tissue injury prevention

and mitigation protocols, the injuries may eventually progress to form large subcutaneous cavities which eventually break through the surface and reveal themselves as stage III or IV pressure ulcers [8], [9].

Currently, the only tool capable of readily detecting early deep tissue injuries is T_2 -weighted MRI [6], [10]. Unfortunately, MRI is not cost-effective for detecting the onset of DTI in a clinical population. Alternately, ultrasound is a much more cost-effective, if less sensitive imaging modality. While it has been shown that some DTI may be discerned using classical b-mode ultrasound imaging [3], [11], the sonographic features of DTI are difficult to separate from regular tissue inhomogeneities. To overcome this, ultrasound elastography may provide more reliable results by imaging the mechanical tissue stiffness rather than its acoustic properties. Ultrasound elastography is an imaging modality which utilizes sonographic techniques to determine the localized mechanical stiffness of tissue and is currently used clinically to detect breast and prostate cancer lesions [12], [13] as well as liver fibrosis [14]. It is known that as DTI form, they undergo mechanical stiffness changes throughout their progression [9], [15], [16], with tissue undergoing significant 1.8 – 3.3-fold mechanical stiffening during injury formation [5]. Initially damaged tissues show signs of increased relative stiffness due to edema-related swelling, while eventually showing signs of decreased relative stiffness due to decomposition and necrosis [17]. Since ultrasound elastography is capable of imaging these stiffness changes, it follows that the formation and progression of DTI may be imaged using ultrasound elastography. In fact, ultrasound elastography has shown to be a valid technique for imaging the formation of a DTI in a rat model [18]. Before this technique can be fully understood and used in human patients, the various parameters involved in performing ultrasound elastography must be characterized with respect to detecting DTI in humans.

1.2 Objective

The broad objective of this work was to numerically characterize the use of ultrasound elastography to detect and monitor formative and progressive deep tissue injuries. Although it has been shown that ultrasound elastography is capable of imaging DTI [18], the degree of suitability of this technique with regard to DTI is not yet understood. When the effect of numerous interrogation parameters on detection sensitivity and ability is known, the technology may be evaluated on its feasibility and usefulness to detect deep tissue injuries. The ultimate goal of this characterization is to be the first stage in the process of allowing ultrasound elastography to be implemented clinically for detecting DTI. It is reasoned that if early detection modalities are implemented clinically, both patients and the health care system may benefit by lowering the incidence and outright cost of treating fully-formed deep tissue injuries.

1.3 Methodology

In order to investigate the use of ultrasound elastography for the detection of deep tissue injuries, the technology must first be characterized and fully understood. While traditional experimentation provides an opportunity to work with physical subjects it can be severely limiting as absolute control over all investigated parameters is relinquished. Further, subject recruitment may present an insurmountable barrier to the execution of such a study. As such, in this exploratory work, various numerical models of the technology have been utilized to investigate the controlled effect of a broad number of parameters relating to each technology. Specifically, k-space models of ultrasonic wave propagation and finite-element models of tissue deformation have been developed. These models were coupled with tissue strain estimation algorithms to

fully simulate the ultrasound ultrasound elastography procedures. Parametric studies on the detection sensitivity and ability of the various ultrasound elastography procedures were carried out with respect to various lesion and technological parameters. Chief parameters of interest included those related to the physical realities of deep tissue injuries such as lesion depth, size, and relative mechanical stiffness as well as parameters related to the design and development of appropriate ultrasonic transducers such as probing frequency, transducer f-number, etc.

1.4 Thesis Outline

In this work, three methods of ultrasonic elastogram image formation have been investigated: quasi-static ultrasound elastography, acoustic radiation force impulse imaging, and shear wave speed quantification. While all three methods may be used to interrogate tissue stiffness, each does so in a distinctively unique way. The academic background leading to the motivation for this work and the development of the numerical models is presented in Chapter 2.

Quasi-static ultrasound elastography estimates tissue strain by tracking inhomogeneities across pre- and post- compression b-mode scans where the compression is generated by manual indentation of the transducer against the surface of the skin. To investigate this technique, two-dimensional b-mode ultrasound scans of simulated pre- and post-compression tissue were generated. A finite-element model of tissue deformation was utilized to generate the post-compression simulated scans. A published tissue strain estimation algorithm was utilized to then generate elastograms for the parametric study. The models and results are presented in Chapter 3.

blurb about ARFI here..

blurb about shear here..

Finally, the results presented in this work and their implications along with suggestions for future work are discussed in Chapter 6.

Chapter 2

Literature Review

In order to understand the need for a clinical method of detecting deep tissue injuries, the full scope and current state of the issue must be explored. To this end, the current state of the literature regarding deep tissue injuries, how they form, what factors characterize them, and how they are currently treated is explored here. In order to relate this disease to the detection modality proposed in this work, the mechanics and history of ultrasound elastography are also explored and related back to the problem at hand. The major gaps in the current literature regarding the use of ultrasound elastography for detecting and monitoring deep tissue injuries are presented as these gaps are what this work attempts to begin to fill.

2.1 Deep Tissue Injuries

Pressure ulcers, commonly referred to as “bedsores”, are an extraordinarily large problem facing the health care system today. At least \$11 billion is spent in the United States of America alone treating approximately 500,000 injuries annually [19], [20] while only a minute fraction of that is spent toward pressure ulcer research [21]. Compared to hospital stays for all other conditions,

patients with at least a secondary diagnosis of a pressure ulcer were more often discharged to a long-term care facility and more likely resulted in death [20]. These injuries place an extremely significant burden on the people who suffer from them—pressure ulcers were found to have a profound impact on people’s lives including: altering their physical, social, and financial status; changing their body image; losing independence and control; and subjecting them to the grieving process [22], [23]. ^{c1}These debilitating wounds are often suffered by people with limited mobility such as those undergoing lengthy surgical procedures, the elderly, and those with spinal cord injuries (SCI) [1]—approximately 80 % of people with spinal cord injuries (SCI) will develop at least one pressure ulcer during their lifetime [2] and approximately 19 % of elderly patients in long-term care facilities will develop one [24]. Pressure ulcers exist throughout the entire health-care system and are often formed when undergoing hospitalization [25]. These injuries have a tendency to become chronic, non-healing wounds and many patients die from complications related to them [26]. Further, patients who have developed at least one pressure ulcer in their life are at a significantly greater risk of developing a second [27]. Pressure ulcers and deep tissue injuries generally form at the bone-muscle interface deep in the tissue [3] with approximately 64 % occurring over the ischial tuberosities, trochanter, or sacrum [28]. In general, these injuries are characterized by a some manner of tissue loss through necrosis of the tissue, though there is currently some debate on the exact nature of these wounds as well as the accuracy of the clinical descriptions attributed to them by the National Pressure Ulcer Advisory Panel (NPUAP).

The NPUAP defines pressure ulcers as a “localized injury to the skin and / or underlying tissue usually over a bony prominence, as a result of pressure, or

^{c1} KH: I already mentioned this in the introduction, verbatim. Where should it go?

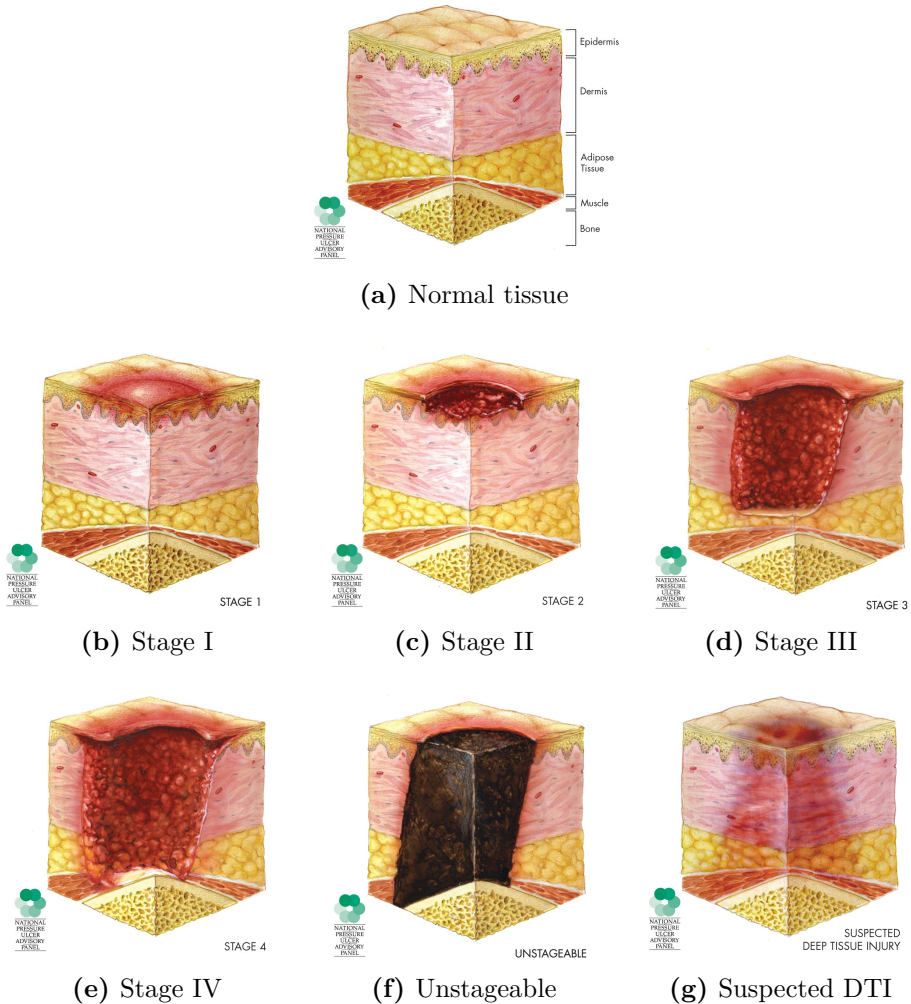


Fig. 2.1: The NPUAP staging guideline illustrations of the various stages / severities of pressure ulcers.

pressure in combination with shear and / or friction” and are generally staged according to a tiered system of increasing damage [7]. The various stages are depicted in Fig. 2.1 and described as follows:

Suspected Deep Tissue Injury

Purple or maroon localized area of discoloured intact skin or blood-filled blister due to damage of underlying soft tissue from pressure and / or shear. The area may be preceded by tissue that is painful, firm, mushy, boggy, warmer or cooler as compared to adjacent tissue.

Stage I

Intact skin with non-blanchable redness of a localized area usually over a bony prominence. Darkly pigmented skin may not have visible blanching; its colour may differ from the surrounding area.

Stage II

Partial thickness loss of dermis presenting as a shallow open ulcer with a red pink wound bed, without slough. May also present as an intact or open / ruptured serum-filled blister.

Stage III

Full thickness tissue loss. Subcutaneous fat may be visible but bone, tendon or muscle are not exposed. Slough may be present but does not obscure the depth of tissue loss. *May* include undermining and tunnelling.

Stage IV

Full thickness tissue loss with exposed bone, tendon or muscle. Slough or eschar may be present on some parts of the wound bed. Often include undermining and tunnelling.

Unstageable

Full thickness tissue loss in which the base of the ulcer is covered by slough (yellow, tan, grey, green, or brown) and / or eschar (tan, brown or black) in the wound bed.

The NPUAP's definitions of pressure ulcers come from clinical experiences with them and are largely based on the ulcer's appearance after they have formed and do not necessarily reflect the true aetiological factors that lead to these conditions. For example, a significant body of literature scientifically

describes deep tissue injuries as being much more insidious than a “localized area of discoloured intact skin” and suggests that many Stage III and IV pressure ulcers are actually advanced deep tissue injuries rather than advanced Stage I or II ulcers [17]. This chasm between the clinically accepted and scientifically observed definitions of deep tissue injuries is likely due to the lack of any clinical detection ability [29]. What is agreed upon is that deep tissue injuries are a major problem and more needs to be done to facilitate preventing and treating them [30], [31] and one of the largest hurdles to preventing and treating DTI is the lack of any substantial early detection ability [32], [33].

2.1.1 Aetiology and Histology

Deep tissue injuries are thought to occur through the combinatory effects of three distinct but related mechanisms: ischemia, insufficient lymph drainage, and cell deformation. Ischemia is a condition where the blood supply to tissue has been cut off, rendering the tissue unable to function appropriately. Insufficient lymph drainage refers to how waste products may accumulate in tissue when the lymph vessels that normally carry them away become occluded. Cell deformation occurs when mechanical strains are imparted upon the tissue, causing excessive deformation in not only the extracellular matrix, but in the cells as well. Taken together, the presence of these factors has been shown to greatly increase the risk of developing a deep tissue injury [4].

For quite some time, ischemia was regarded as the chief acute risk factor for developing late-stage pressure ulcers [34]–[36]. Although studies have shown that healthy tissue is able to survive complete ischemia for approximately 4 hours before severe necrosis set in [37], [38], deep tissue injuries are clinically found when loading times are substantially less than this [25], [39]. The model of ischemic damage alone could not account for the rate of late-stage pressure

ulcers that we were witnessed.

Once it was realized that ischemia alone could not be the culprit behind deep tissue injury formation, ischemia-induced reperfusion injury became implicated in the formation of DTI [40]–[42]. An ischemia-induced reperfusion injury is caused when blood is allowed to flow back into a region of tissue that was previously ischemic. While seeming somewhat contrary to its expected effect, the restoration of circulation results in a swelling and inflammatory effect which causes extensive microvascular damage [41]. The effect of reperfusion was confirmed when comparing pure ischemic conditions in tissue to a cycle of ischemic-reperfused conditions over the same period of time, where it was found that significantly greater damage was caused by repeated loading-unloading rather than simple constant loading [42], [43]. While ischemia-reperfusion injuries provide a more complete explanation about the formation of deep tissue injuries, they still do not account for those injuries acquired under constant pressure over short time periods.

In order for cells to function in a healthy manner, the waste they produce must be constantly carried off and processed via the lymphatic system and its series of lymph vessels that perfuse tissue. If the magnitude of pressure applied to tissue reaches a threshold level, the pressure occludes the lymph vessels and lymphatic drainage ceases [44]. Once lymphatic drainage ceases, cell waste accumulates in the tissue and is thought to initiate necrosis in the cells [45]–[47]. Since this model of damage relates to occlusion of vessels, inhibited lymphatic drainage may be categorized as an ischemic risk factor.

In order to account for deep tissue injuries that form over short time periods, a model of cell deformation leading to necrosis has more recently been proposed [48]–[50]. It has constantly been observed that tissue regions which eventually form deep tissue injuries exhibit signs of locally increased strains

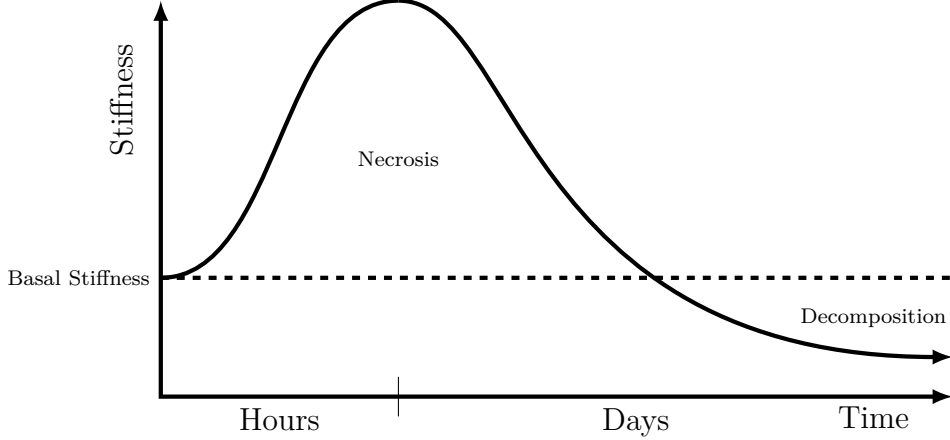


Fig. 2.2: Schematic representation of the time course of tissue stiffness changes in a deep tissue injury site. The estimate for the time-course for local rigor mortis was obtained from animal model studies [60] and the estimate for the time-course for tissue decomposition was obtained from the forensic literature [59]. (Adapted from Gefen [17])

[10], [16], [51]–[53], with greater degrees of deformation correlating to greater degrees of damage. To account for these results, it has been proposed that excessively deforming strains applied to cells over extended periods of time can alter the permeability of the cell's plasma membranes, leading to an overall reduced cell viability [54]. Further, it has been shown both in finite-element models and experimentally that the stiffness of soft tissue and the corresponding strains that are developed within them are closely related [5], [55]–[57]. Not only does the amount of deformation depend on the stiffness of tissue, but the stiffness of tissue was found to correlate to the level of deep tissue injury damage seen in the resulting histology [58] with immediate 1.6-fold to 3.3-fold stiffening of the tissue occurring immediately after injury [5], [15]. Further, the stiffness of tissue severely drops below that of healthy tissue when it begins to decompose [5], [59], leading to a relationship between injury progression and stiffness as shown in Fig. 2.2 (adapted from [17]).

There have been many models of deep tissue injury formation throughout the years, each relating to different mechanisms, though all relating to me-

chanical stress of the tissue, either through vessel occlusion or direct cellular strain. The truth is most likely a combination of these effects, with cell deformation dominating the damage on shorter time scales with increased applied pressure and vessel occlusion type injuries dominating on longer time scales [4]. In order to further investigate the etiology of PU and DTI, a combination of experimental and numerical studies has been suggested to provide better fundamental knowledge besides existing clinical experience [8]. There is also significant evidence in the literature that suggests that the current NPUAP definitions of PU and DTI are unacceptable and not based on scientific evidence and that updating the clinical definitions to better reflect what exists in the literature is crucial to increasing the success of diagnosis and treatment of PU and DTI [17], [29].

2.1.2 Detection

As previously mentioned, there is a lack of means for detecting the early onset of deep tissue injuries in a clinical setting [32], [33]. Currently, when attempting to detect and diagnose a deep tissue injury or pressure ulcer, clinicians generally rely upon a risk-factor scale for patients rather than actually detecting a lesion. Popular risk assessment tools include the Norton, Braden, and Risk Assessment Pressure Sore scales which each attempt to predict the formation of a pressure ulcer in a patient given their scores in a series of relatively subjective variables such as “general physical condition” and “mental state” [61]–[63]. Aside from these main risk-assessment scales, multiple other scales have been proposed for specific populations such as SCI patients [2] and oncology patients [64]. While these tools assist health-care practitioners to manage their limited resources with regards to patient care, at best they only provide guesses as to who will develop pressure ulcers or not. The sensitivity—the

ability to correctly diagnose an existing condition—of these techniques ranges from approximately 42 % – 87 % while the specificity—the ability to correctly determine that no condition is present—ranges from 57 % – 88 % [65]. Other studies have shown that nurses have great difficulty detecting and diagnosing suspected deep tissue injuries given the current frameworks they are provided [66], while physicians are even worse [67]. While these scales are “better than nothing” at diagnosing patients with pressure ulcers, they are far from ideal and are simply not capable of actually diagnosing this disease—for that, a quantifiable detection technology is required.

In pressure ulcer research it is common to evaluate the extent of deep tissue injury formation through the use of T_2^* -weighted MRI [6], [10], [16]. T_2^* -weighted MRI is able to detect deep tissue injury by investigating tissue oxygenation as a proxy for detecting the lack of cellular activity due to necrosis. Although this technique is well suited for research purposes, it is simply not viable for detecting and monitoring the progression of DTI in the large population of at-risk patients. At the time of writing, MRI scans can easily cost upwards of \$1,000 and take over an hour to complete ^{c1}. Further, patients with implants such as pacemakers and who make up a large proportion of the at-risk population cannot undergo MRI scans due to the large magnetic forces involved and / or the need to relocate from their hospital bed to the stationary MRI machine. Of the alternative diagnostic imaging modalities that currently exist, ultrasound provides the most promise due to its ability to non-invasively interrogate tissues in a mobile and cost-effective manner.

B-mode ultrasound scans involve the sonographic interrogation of a tissue’s acoustic properties by transmitting sound waves on the order of multiple MHz and “listening” to the waves as they are reflected in tissue. B-mode ultra-

^{c1} KH: Citation needed!

sound imaging has been used to identify hypo-echoic regions in sub-epidermal tissue related to DTI [3], [11], [68], however the results from these studies are somewhat unclear and require a degree of interpretation of the results. After combining thermographic techniques with b-mode imaging results, it may be possible to increase the accuracy of early deep tissue injury detection [69]. As a more reliable alternative, ultrasound elastography—a sonographic technique for interrogating tissue strains rather than acoustic properties—has been proposed as a possible tool for clinical diagnosis of DTI [17], [70], [71]. Some exploratory studies have successfully used this technique to quantify deep tissue injury formation not only numerically, but in PVA-cryogel phantoms as well as in a rat model [18], [72]. While these studies show promise, they are only the beginning for the adoption of ultrasound elastography as a viable clinical detection modality for deep tissue injuries.

Recently, another possible avenue for DTI detection has arisen which lies in the biochemical markers present in a patient’s blood or urine. Rhabdomyolysis refers to the process when myoglobin proteins from damaged skeletal muscle enter the bloodstream due to a breakdown of muscle fibres in the body. Although this condition may be caused by numerous factors such as hyperthermia, ingestion of various drugs, alcohol abuse, toxins, autoimmune disease, or physical damage [73], [74], it may also be an indicator of formative DTI in at-risk patients who do not present with any of the aforementioned risk factors. Myoglobin proteins present in the blood get filtered in the kidneys and as such can present in the urine, turning it tea-brown [75].

With the many avenues of DTI detection currently being explored and utilized, it is most likely that a combination of all the techniques will provide the most utility. For example, upon hospital admission or with a reasonably high risk assessment score, a patient may be given a blood test which confirms the

presence of a forming injury or not. Patients with forming injuries may then be scanned using ultrasound technology to locate and quantify the injury. That patient may then receive more targeted care, of which the effectiveness may be continually monitored using both blood and ultrasound tests. It is expected that the targeted care that this approach would provide would increase patient health and well-being while at the same time decreasing the overall load on the health-care system.

2.1.3 Prevention and Treatment

The current state of deep tissue injury treatment and prevention largely reflects the lack of a quantifiable detection modality. One of the most commonly used preventions is called “turning” whereby patients are repositioned in their beds or wheelchairs such that individual regions of tissue are intermittently relieved of pressure. Although commonly implemented in health care settings, turning has repeatedly been found to be inadequate at reducing the incidence of pressure ulcers [76], [77]. A more technological means of reducing the mechanical loads on tissue lies in support surface design [78]. Unlike turning, pressure-redistribution foam mattresses have repeatedly shown their ability to reduce the incidence of pressure ulcers in a cost-effective manner [79], [80]. Despite the effectiveness of these surfaces however, the overall prevalence rate of pressure has not changed significantly, suggesting that appropriate preventions are not being utilized in health-care settings [31].

An emerging technology in the realm of pressure ulcer prevention is intermittent electrical stimulation (IES). IES is the process by which electrical impulses are utilized to activate muscle fibres and contract the muscle. IES has been found to not only increase the oxygenation in deep tissue [81], but also significantly reduce the damage caused from excessive loading [82]. While

still being developed, IES may prove to be an extremely effective preventative therapy for DTI.

While various technologies exist or are in development for preventing pressure ulcers, little is available to treat them when they occur. Generally, pressure ulcer treatment involves optimizing regional blood flow, managing underlying illnesses, and providing adequate nutrition [26]. If a pressure ulcer has become chronic, treatment switches to controlling the symptoms and preventing complications [26]. Negative pressure wound therapy is a process by which a slight vacuum is applied to the open wound for several weeks and has shown some success in reducing the severity of late-stage pressure ulcers [83]. Surgical techniques such as debriding may also be used in an attempt to remove necrotic tissue from the wound and prevent it from growing any larger [84], [85]. Skin-flap surgery is often used on chronic ulcers in an attempt to protect the wound bed [86].

When various prevention and treatment paradigms are implemented, the incidence of hospital-acquired pressure ulcers may decrease dramatically [87]–[89]. However, one of the key required areas of improvement is in the detection and monitoring of pressure ulcers [33]—without the ability to continually monitor a wound, the true effectiveness of any given therapies is indeterminate.

2.2 Ultrasound Elastography

Ultrasound elastography is a relatively new imaging modality which is capable of imaging the stiffness of soft tissue using ultrasound waves and has its roots in the clinical practice of manually palpating tissues to detect localized changes in the mechanical properties of the tissue [90]. In general, the principle of ultrasound elastography is to visualize the deformation of soft tis-

sue scattering centres in response to an externally applied compressive force [91]. This is in contrast to traditional ultrasound images which are created by interrogating tissue with high-frequency acoustic waves and “listening” to their echoes as they reflect off of tissue boundaries and small tissue irregularities (scattering centres) [92]. The externally applied force in ultrasound elastography may come from manual indentation of the ultrasound probe, a secondary external vibrator, or as an acoustic radiation force impulse (ARFI) generated by the ultrasound transducer itself [90]. There are generally three distinct methodologies or algorithms for generating soft tissue elastograms: quasi-static methods which rely upon the manual indentation of the transducer probe, ARFI imaging which measures the dynamic response of tissue due to ARFI excitation, and shear wave speed quantification which measures shear wave speeds developed in tissue due to ARFI excitation.

Ultrasound elastography is a proven technology when it comes to detecting very stiff lesions against relatively soft backgrounds—it has successfully been used to detect breast and prostate cancer lesions [12], [13] which are several orders of magnitude stiffer than healthy tissue as well as liver fibrosis [14].

2.2.1 Quasi-Static Ultrasound Elastography

2.2.2 Acoustic Radiation Force Impulse Imaging

2.2.3 Shear Wave Speed Quantification

2.3 Conclusion

Chapter 3

Numerical Characterization of Quasi-Static Ultrasound Elastography

3.1 Introduction

The goal of this study was to numerically characterize various important parameters related to detecting DTI using quasi-static ultrasound elastography (such as lesion geometry, material properties, and transducer characteristics) in order to examine the feasibility of using the technique to detect early DTI in humans. Quasi-static ultrasound elastography involves displacing the surface of the skin such that internal tissues are placed under a strain field. Ultrasound signals are used to track internal strains which then relate to the localized mechanical stiffness of the tissue—local regions that are significantly more or less stiff than surrounding tissue may be classified as either undergoing rigor mortis or necrosis and may present cause for concern.

3.2 Method

In order to evaluate the sensitivity of using quasi-static ultrasound elastography to detect deep tissue injuries, a numerical model of these injuries was created such that a subset of the investigated cases mimicked a physical phantom model which was used for validation. This numerical model allowed the rapid modification of numerous parameters related to DTI to examine their effect on the method’s detection sensitivity where detection sensitivity is defined as the slope of the given characterization plot. An ideal detection sensitivity would resemble a unary mapping between the measured lesion stiffness ratio and the true lesion stiffness ratio. Lesions are considered to be “detectable” when the measured strain ratio of the lesion is significantly greater than or less than 1. Lesions with measured strain ratios of 1 would appear the same as healthy tissue and would most likely not be detected in the elastogram. To fully understand the problem, 5 general model cases were studied with each case generating numerous sub-studies on the effect of various parameters relating to that case. These parameters included: lesion depth; lesion altitude (distance of the lesion above deep bone); lesion diameter; ratio of the stiffness between the lesion and the surrounding tissue; ultrasound probing frequency; strain level applied by the transducer; the separation distance between two co-located lesions; radius of a circular averaging filter applied to the lesion boundaries; the number of smaller clustered lesions per unit area—noting that the small lesions in this model may overlap each other; the radius of each individual clustered lesion; the width of the lesion in a Visible Human [93] model and the depth of the lesion in a Visible Human model. The range of values for the tested parameters are given in Table 3.1 which resulted in a total of 144 model cases that were analyzed. The geometry of the models shown in Fig. 3.1 include: a cross-section of a simple spherical lesion embedded

Table 3.1: Range of values of investigated parameters

Parameter	Symbol	Values
Lesion depth	d	[3.5, 6.5, 8.5, 10.0] cm
Lesion altitude	h	[1.25, 2.50, 3.75] cm
Lesion diameter	ϕS	[0.5, 1.0, 2.0, 2.5] cm
Lesion stiffness ratio	E_{rel}	[0.32, 0.56, 1.80, 3.20]
Ultrasound frequency	f	[2, 4, 8] MHz
Transducer-applied strain	ε_{app}	[2.5, 5.0, 10.0] %
Co-located separation distance	δ_{sep}	[1.25, 1.50, 1.75, 2.00] cm
Blurred lesion blur radius	b_r	[1.0, 2.5, 5.0, 7.5] mm
Clustered lesion density	b_ρ	[10, 20, 30, 40] cm ⁻²
Clustered lesion radius	r_{bl}	[0.5, 1.0, 1.5] mm
Visible human lesion width	ϕS	[0.5, 1.0, 2.0, 2.5] cm
Visible human lesion depth	d	[6.25, 6.75, 7.25] cm

within a 2-dimensional rectangular zone of soft tissue; two lesions located at the same depth separated laterally by a finite dimension, δ_{sep} ; a cross-section of a spherical lesion without hard boundaries; a cluster of small lesions which together form a larger lesion area; and a lesion with mri-acquired geometry [82] embedded in geometry obtained from a Visible Human slice [93].

In Fig. 3.1e, the lesion is located superficial to the left ischial tuberosity in the transverse plane. The lesion geometry was obtained from an MRI scan of a real deep tissue injury induced in a porcine model [82]. The generic soft tissue in this model is modelled after muscle, with a layer of adipose tissue residing at the surface of the model.

Note that the axial direction referred to henceforth as the “axial” direction of an ultrasound transducer placed along the top (superficial) surface of the domain such that it becomes the “vertical” direction.

Simulated ultrasound images were acquired through the convolution of a point spread function with a normally distributed background map of scattering centres [94]. These images were then combined with a finite-element deformation model of the strained tissue to generate both pre- and post- com-

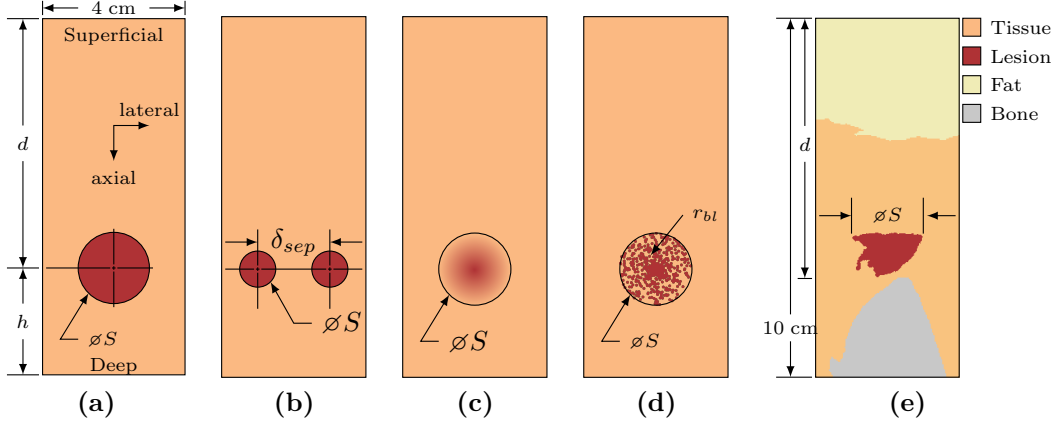


Fig. 3.1: Model geometry showing the investigated lesions embedded in a 4 cm wide soft tissue domain. Axial and lateral directions mimic that of a typical ultrasound transducer placed along the top boundary of the domain. The simplest case of a circular lesion embedded in a soft tissue domain located superior to hard underlying bone is shown in (a). In order to investigate the interference caused by closely-located lesions, the case shown in (b) was investigated. Because of the relatively unknown and variable geometric properties of deep tissue injury lesions, cases (c) and (d) were investigated where the lesion edges were blurred and the lesion was actually a large collection of small lesions, respectively. Finally, to investigate detection sensitivity in a realistic setting, case (e) was investigated where an mri-acquired deep tissue injury was overlaid on a slice from the Visible Human Project such that the injury lesion was located immediately superior to an ischial tuberosity.

pression images of the lesions and surrounding tissue. These images were fed into a tissue strain estimation algorithm to determine the detection sensitivity of the technique. Finally, the technique was validated against a physical phantom model using a subset of the simulated cases.

3.2.1 Formation of B-Mode Ultrasound Images

Through the convolution of a point spread function and a normal random distribution of scattering centres, simulated ultrasound images were generated. The point spread function was defined axially as a cosine function operating at the ultrasound probing frequency modulated by a Gaussian distribution defined by $\mu = 2\lambda$ and $\sigma = 2\lambda$ where λ is the wavelength of the ultrasonic probing waves. Laterally, the point spread function was modelled as a Gaus-

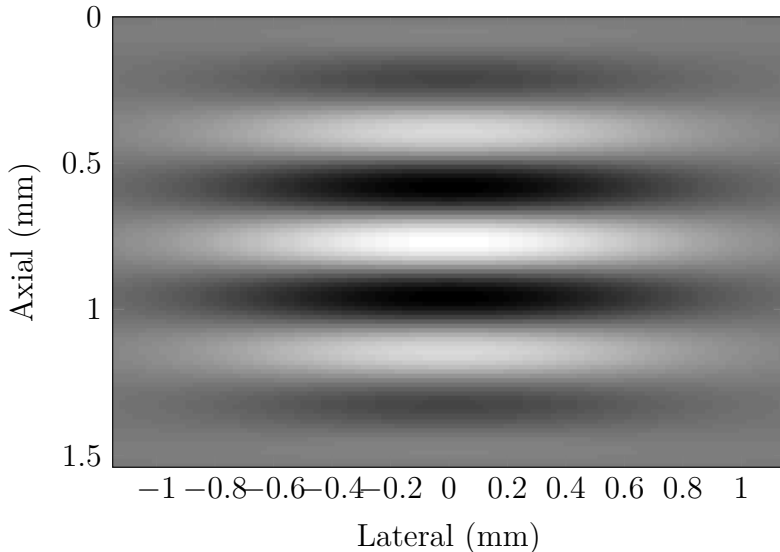


Fig. 3.2: Point spread function used for simulating b-mode ultrasound scans. The function is defined axially by a cosine function at the probing frequency and modulated by a Gaussian function both axially and laterally.

sian distribution defined by $\mu = 0$ and $\sigma = 0.25w_{active}$ where w_{active} is the total width of the active transducer elements during scan-line acquisition. This resulted in the point spread function given in Fig. 3.2. Resulting images were composed of 192 scan lines each sampled at 50 MHz.

3.2.2 Finite-Element Model of Tissue Deformation Under Surface Distortion

As a response to an external load being applied to the boundary of a domain, internal structures deform. In the case of a relatively stiff deep tissue injury embedded within surrounding soft tissues, this implies that when the surface of the skin is depressed, the relatively stiff lesion will not strain to the same magnitude that the surrounding soft tissue does. In order to simulate the deformation of interrogated tissue, the displacement field for the simulated

models was calculated according to:

$$-\nabla \cdot \sigma = F \quad (3.1)$$

Where σ is the Cauchy stress tensor and F are the applied body forces. Simulations were performed assuming a 2-dimensional linearly elastic material deformation model under plane strain conditions. A 3-dimensional model was also considered, however the deformations differed from the 2-dimensional simulation by less than 1% so a 2-dimensional model was deemed adequate. Soft tissue was modelled using a Young's modulus of elasticity of 25 kPa, Poisson's ratio of 0.499, and density of 998 $\frac{\text{kg}}{\text{m}^3}$ [95]–[97]. Bone was modelled in the Visible Human model with a Young's modulus of elasticity of 18.6 GPa, Poisson's ratio of 0.15 and density of 297 $\frac{\text{kg}}{\text{m}^3}$ [98]–[100]. The only difference in lesion mechanical properties from the surrounding soft tissue was the modulus of elasticity which varied according to the simulation parameters. The bottom of the domain was held fixed such that:

$$u = 0, \quad \Gamma = \Gamma_{bottom} \quad (3.2)$$

While this boundary condition represents an idealized scenario, it may be likened to that of tissue located superficial to a relatively stiff anchoring bone below since the stiffness of bone is several orders of magnitude greater than soft tissue and will not significantly deform under the loads explored in this model. This lower region is where deep tissue injuries generally form and is therefore of special importance. Compressive strains were applied to the top of the domain so as to induce strain along the top boundary:

$$u = (0, -u_0), \quad \Gamma = \Gamma_{top} \quad (3.3)$$

From these simulations, displacement fields throughout the domain were calculated which were then used to displace tissue (including scattering centres) in the simulated ultrasound images in both the axial and lateral directions. This process resulted in pairs of pre- and post- compression simulated b-mode images of lesions of varying parameters which could then be analyzed and characterized.

3.2.3 Characterizing Quasi-Static Ultrasound Elastography

Utilizing a 2-D locally regularized tissue strain estimation algorithm [101], pairs of pre- and post- compression images were used to calculate elastogram estimations for the full range of parameter values of the simulated lesions. The algorithm consists of sweeping the image domain with a series of overlapping regions of interest (ROI). ROI are compared between pre- and post-compression images, with ROI in the post- compression images being axially scaled and translated and laterally translated versions of the same ROI in the pre-compression images.

Qualitatively, the noise and computation time of the resulting elastograms were found to be minimum when using an axial ROI size of approximately 10 times the ultrasound wavelength. Axial ROI overlap was held at 99 % to produce elastograms with minimal noise, even though this introduced significant increases in computation time. Due to the extreme anisotropic nature of ultrasound signals, lateral ROI size was kept to 5 signal widths with lateral ROI overlaps of 80 %.

Table 3.2: CIRS Phantom Model Mechanical Properties

Property	Value
Nominal basal stiffness	25 kPa
Lesion stiffness	[8, 14, 45, 80] kPa
Speed of sound	1,540 $\frac{\text{m}}{\text{s}}$
Acoustic attenuation	0.5 $\frac{\text{dB}}{\text{cm MHz}}$
Lesion diameter	[10, 20] mm
Lesion depth	[15, 35] mm

3.2.4 Model Validation Using a Commercially Available Phantom

Utilizing a CIRS Elasticity QA Phantom model 049, a subset of the results obtained from the finite-element simulations and numerical characterizations were compared against their physical phantom equivalents. The phantom mimics acoustically homogeneous soft tissue with embedded lesions which vary in depth, size, and mechanical stiffness. Mechanical properties of the phantom as given by manufacturer specifications are summarized in Table 3.2. Pre- and post- compression b-mode ultrasound images were obtained of each lesion in the phantom and the resulting strain ratio for that lesion was compared to the simulated strain ratio for that combination of parameters. Specifically, lesions at a depth of 3.5 cm, a diameter of 2.0 cm, and with true stiffness ratios of 0.56, 1.80, and 3.20 were examined. Surface indentation was performed manually with the transducer indenting approximately 0.5 cm (6.25 %) at the surface.

3.3 Results and Discussion

Following the procedure outlined in Section 3.2, finite-element models of ultrasonic b-mode image formation and tissue deformation were synthesized. The results of these models were then fed into the local strain estimation algo-

rithm described in Section 3.2.3. The resulting numerical characterizations of the relationship between measured and true strain ratios in the simulated tissue and their dependence on the various lesion parameters given in Table 3.1 were examined. Finally, the local strain estimation algorithm was carried out on a physical phantom and compared against a subset of the simulated cases.

3.3.1 Finite Element Models of Ultrasound and Deformation

Sample images generated using both the acoustic and deformation finite-element models are given in Figs. 3.3a – 3.3d. In Fig. 3.3a, a sample generated b-mode ultrasound scan is given. Fig. 3.3b shows the lateral displacement field generated by the deformation finite-element model while Fig. 3.3c shows the axial displacement field. The entire top surface of the model has been displaced axially by 6.25 mm (5 %), which caused deformation of both the soft tissue and embedded lesion within. Since the lesion was modelled as being 3.2 times stiffer than the surrounding tissue, the lesion underwent less strain which consequently resulted in the lesser displacement depicted. Fig. 3.3d shows the resultant b-mode image generated by applying the displacement field given in Figs. 3.3b and 3.3c to the tissue and embedded scattering centres used to create Fig. 3.3a. What results is a locally scaled and translated version of Fig. 3.3a that corresponds to indenting the surface of the skin above a stiff lesion. The large anechoic region located at the bottom of the domain is tissue that was not modelled in the pre-compression image as it was outside of the original domain. This area represents the region of tissue that is undetectable with the strain-estimation algorithm given in Section 3.2.3 as the information contained there is only available in one of the two input images and so is

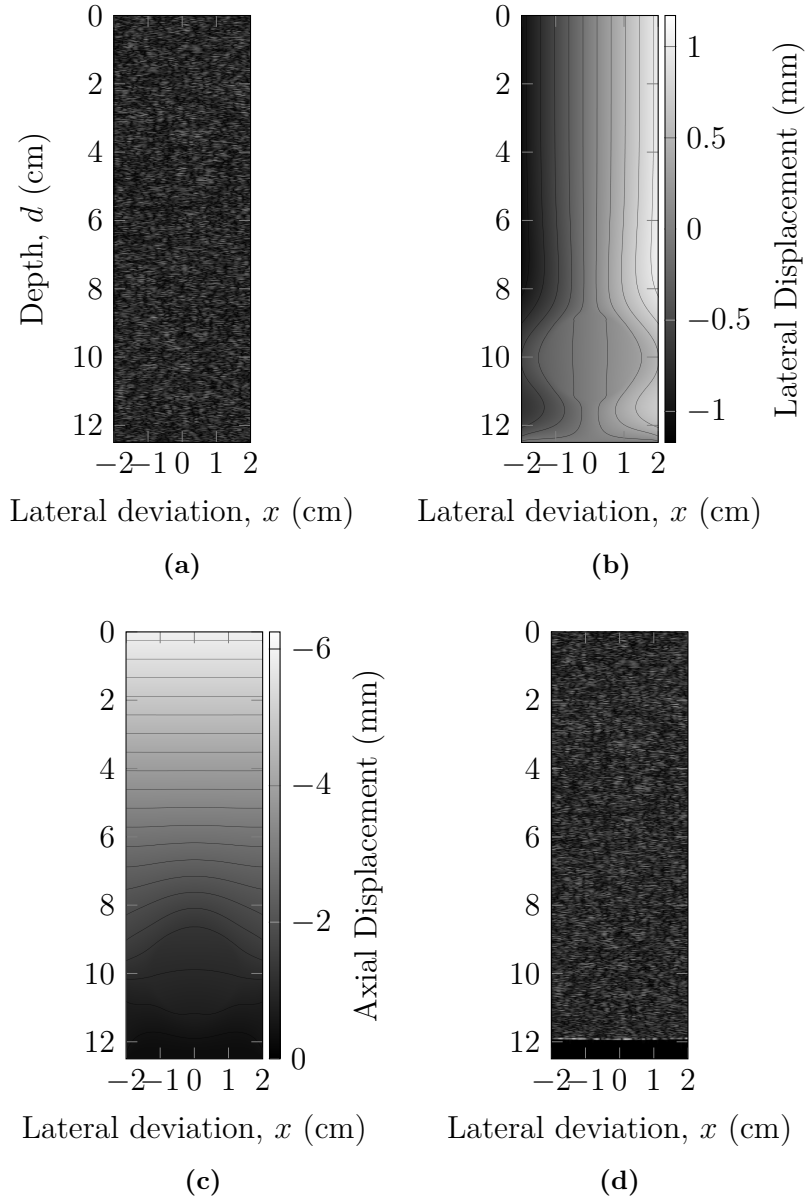


Fig. 3.3: Finite-element model results for the case when $d = 10\text{ cm}$, $\phi S = 2.5\text{ cm}$, $\varepsilon_{rel} = 3.20$, and $f = 4\text{ MHz}$ showing (a) a generated b-mode image of the pre-compressed tissue domain, (b) the lateral displacement field and (c) the axial displacement field induced by compressive strain applied to the top of the boundary, and (d) a generated b-mode image of the post-compressed tissue domain. The included lesion is not visible in (a) and (d) as its acoustic properties were no different than surrounding tissues. An anechoic region is visible along the bottom of the domain in (d) which represents tissue outside of the domain visible in (a).

considered incomplete data.

3.3.2 Resulting Elastograms

The 2-D locally regularized tissue strain estimation algorithm described in Section 3.2.3 was used in combination with the simulated resultant b-mode ultrasound images (Figs. 3.3a and 3.3d) in order to generate elastogram images which were used in the subsequent analysis. An example elastogram resulting from the simulation presented in Fig. 3.3 is shown in Fig. 3.4. Throughout the entire domain on this sample elastogram, regions outside of the stiff lesions showed compressive strains of approximately 5 % as expected due to the compression applied to the upper boundary of the model. The entire lesion region showed relatively consistent low strain amounts of approximately 2.5 %, which is consistent with the lesion being stiffer (and so straining less) than the surrounding tissue. Of note is the increased strain pattern which appeared both axially and laterally around the lesion. While generally symmetric about the axial direction, this stress field was largely concentrated above the lesion when the lesion was deep (close to the bone). This may be explained as a stress concentration brought about by the sudden change in mechanical material properties of the tissue and may serve to fuel the conditions of excessive cell deformation and ischemia which initiated the formation of a deep tissue injury in the first place, exacerbating the wound and assisting its expansion toward the surface. Further, a largely variable strain field artifact is seen along the superior surface of the elastogram shown in Fig. 3.4. While this field does not appear to affect the remainder of the generated elastogram, it will serve to mask any extremely shallow legions in the tissue, though given as deep tissue injuries generally form immediately superior to boney prominences, this is unlikely to be the case. It is hypothesized that this variable strain field may be due to the large deformations present along the superior surface of the domain.

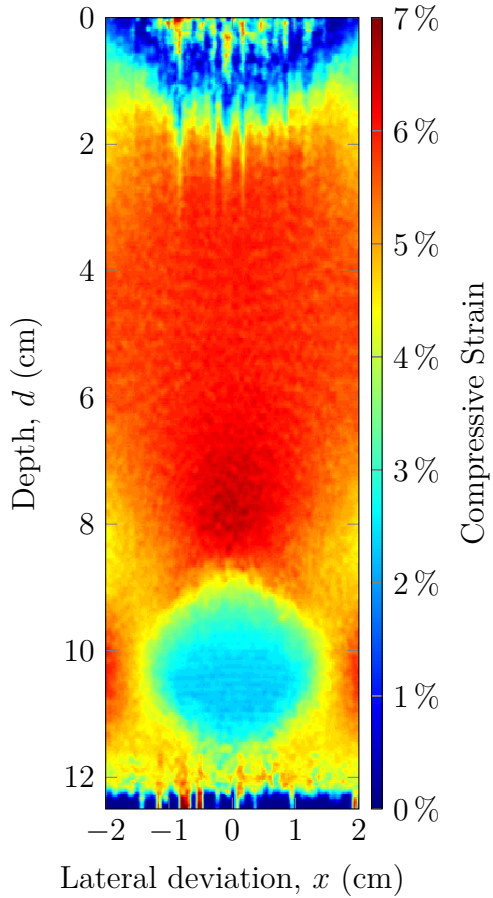


Fig. 3.4: Sample strain elastogram showing estimated strain values for $d = 10$ cm, $\varnothing S = 2.5$ cm, $\varepsilon_{rel} = 3.20$, $f = 4$ MHz. While undetectable on a single b-mode image, the elastogram clearly shows a low-strain (stiff) lesion located approximately 10 cm from the surface.

3.3.3 Numerical Characterizations

In order to determine the sensitivity of using quasi-static ultrasound elastography to detect deep tissue injuries, elastograms such as the example that was calculated in Section 3.3.2 were calculated for the full range of parameters given in Table 3.1. “Measured” strain ratios for each elastogram were obtained by comparing the mean strain within each lesion with the mean engineering strain of the surrounding tissue such that:

$$\varepsilon_{rel,measured} = \frac{\varepsilon_{tissue}}{\varepsilon_{lesion}} \quad (3.4)$$

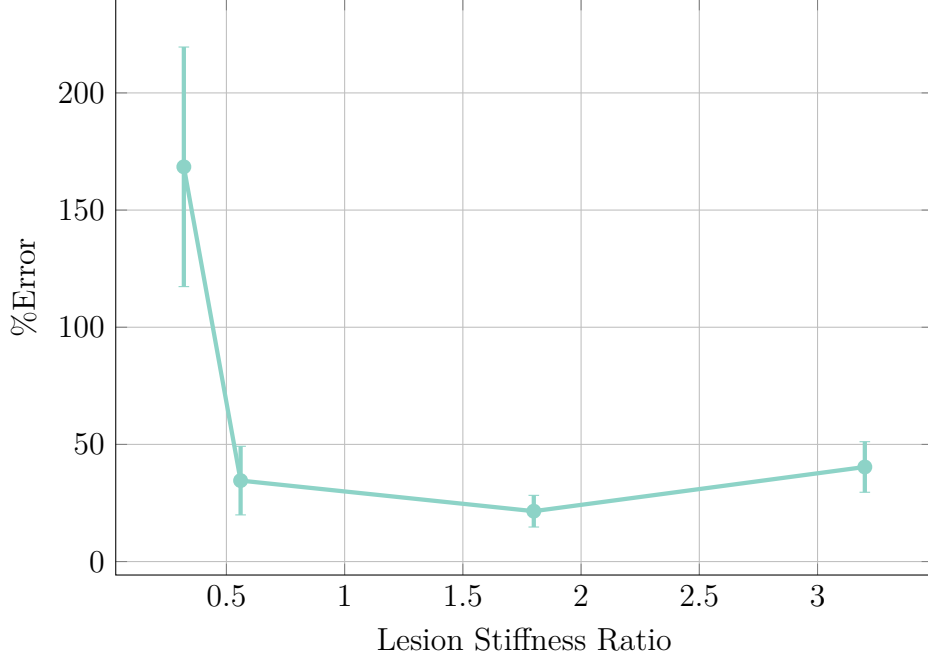


Fig. 3.5: Detection ability as it is related to true lesion stiffness ratio. For all but small lesion stiffness ratios (very soft “lesions”), results are linear and predictable. For small lesion stiffness ratios (0.32), the lesion becomes severely misrepresented. This is likely due to the algorithm “losing track” of scattering centres for the relatively large displacements induced in the significantly less stiff tissue.

ε_{tissue} was sampled as the mean strain in the region of tissue with the same geometry as the lesion located immediately superficial to the lesion in all cases.

In order to characterize how each parameter of interest affects the detection sensitivity of quasi-static ultrasound elastography, measured strain ratios for various lesions were calculated and compared against $\varepsilon_{rel,true}$. $\varepsilon_{rel,true}$ is derived from the relative Young’s modulus of elasticity of the lesion such that:

$$\varepsilon_{rel,true} = \frac{\varepsilon_{tissue}}{\varepsilon_{lesion}} = \frac{\left(\frac{\sigma_{applied}}{E_{tissue}}\right)}{\left(\frac{\sigma_{applied}}{E_{lesion}}\right)} = \frac{E_{lesion}}{E_{tissue}} \quad (3.5)$$

Fig. 3.5 portrays the severe error involved with using the methods described in Section 3.2 to investigate extremely low stiffness lesions. In nearly all investigated cases where the true lesion stiffness ratio was 0.32, the algorithms described severely misrepresented the measured strain ratio of the

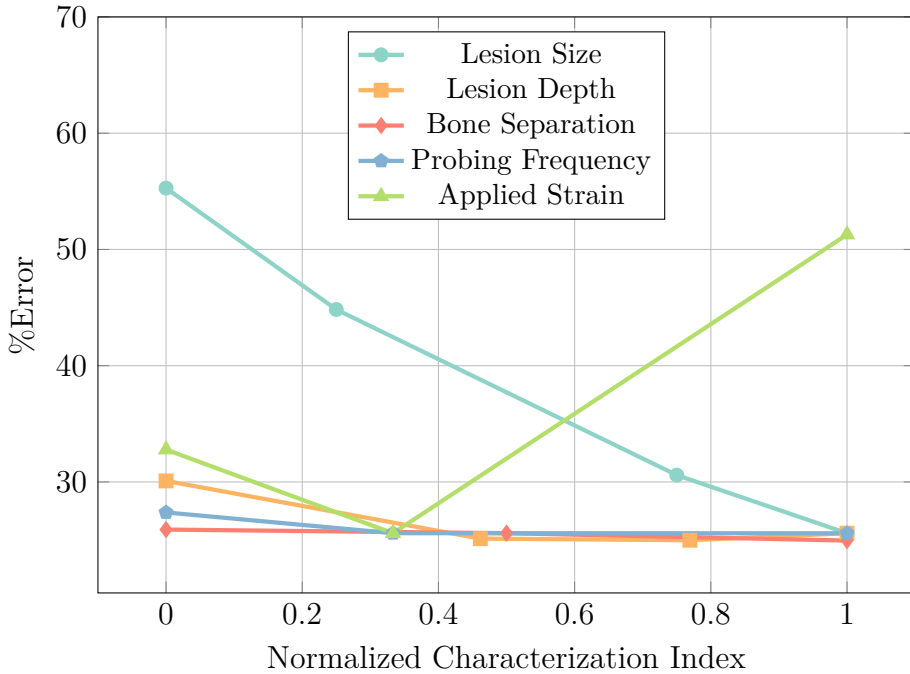


Fig. 3.6: Error characterization for range of studied parameters for the simple model of a spherical lesion embedded within soft tissue as seen in Fig. 3.1a. Each parameter has been normalized to the range studied so overly-sensitive regions may be readily distinguished.

lesion, often portraying these extremely low stiffness regions as being more stiff than they truly were. It is hypothesized that the excessively large localized deformations in these lesions interrupted the algorithm's ability to sufficiently track the displacement of scattering centres within the tissue, lowering the magnitude of displacement within the lesion and subsequently increasing its “measured” strain ratio.

In order to broadly investigate the critical parameter-values of the investigated models, each parameter was normalized to its investigated range and the error resulting over these ranges is given in Figs. 3.6 and 3.7.

In Fig. 3.6, it is clear to see that the most sensitive error-inducing situations occur when either the lesion is very small or if large strains are used to deform the tissue. Similarly, it is expected that if the lesion depth were increased much further, significant errors would arise with increasing depth.

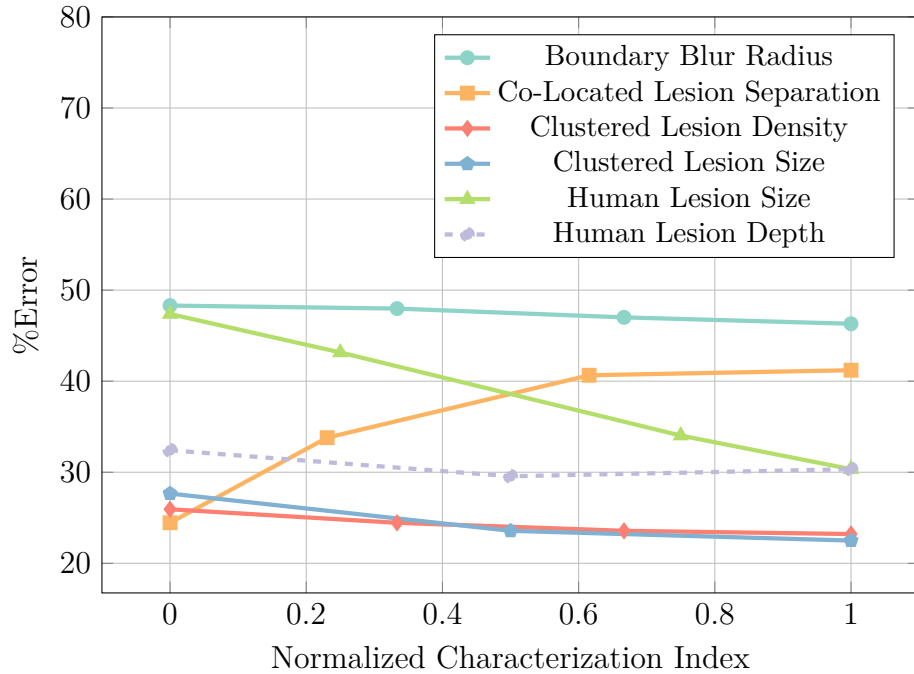


Fig. 3.7: Error characterization for range of studied parameters for the co-located lesions, blurred boundary lesions, clustered lesions, and visible human lesion models as seen in Figs. 3.1b – 3.1e. Each parameter has been normalized to the range studied so overly-sensitive regions may be readily distinguished.

Logically, this may be explained due to the decreasing magnitude of displacement with increasing depth—at a certain point, the magnitude of displacement of scattering centres will be on par with the measurement noise, and the lesion will cease to be detectable.

From Fig. 3.7 it can be seen that small lesions in the Visible Human-MRI model as well as co-located lesions with large separation distances produce greater measurement errors. Conversely, lesion depth in the Visible Human-MRI model; lesion density and individual lesion size in the clustered lesion model; and boundary blur radius in the blurred-edges model do not seem to affect the measurement error significantly. Of note is the relative large amount of static error present in the boundary blur radius model which is hypothesized to be due to lesser mean tissue stiffness in the investigated region than expected.

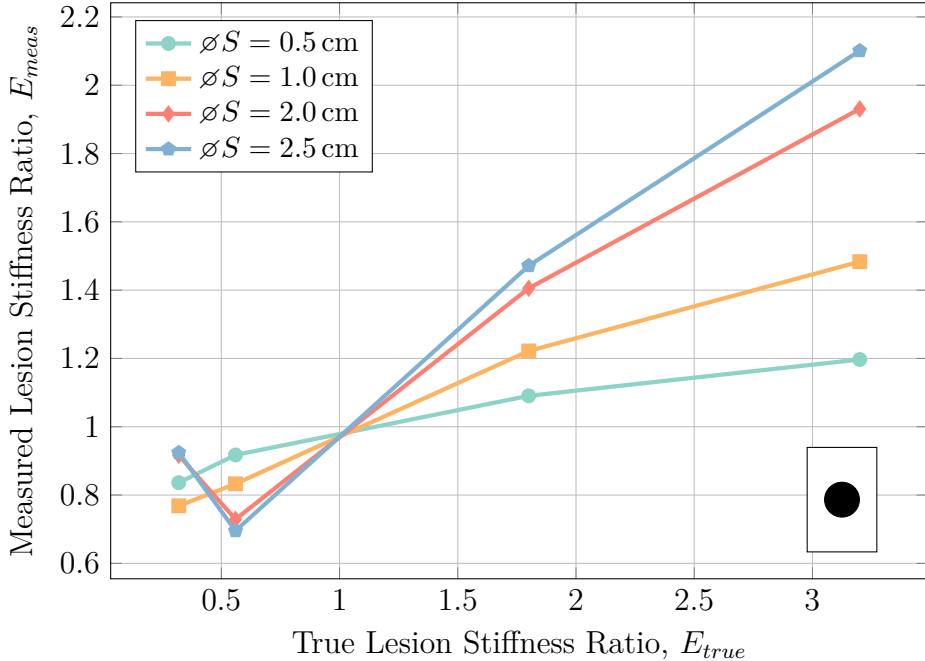


Fig. 3.8: Lesion size characterization at a depth of 10 cm with a 4 MHz ultrasound probing frequency showing increasing detection sensitivity of the lesion with increasing lesion size. Detection sensitivity is less than ideal for all cases, with the best case being for lesions approximately 2.5 cm in diameter.

Fig. 3.8 shows the relationship between lesion size and detection sensitivity for lesions at a depth of 10 cm in a model depth of 12.5 cm interrogated at 4 MHz with 5 % applied strain. Specifically, Fig. 3.8 shows the decreasing detection sensitivity with decreasing lesion size with the best detection sensitivity being with the largest investigated lesions with a diameter of 2.5 cm. On the opposite end, the detection sensitivity of lesions at or below 0.5 cm in diameter is questionable. Although data is lacking on the true size of formative DTI, MRI results indicate that untreated DTI are on the scale of multiple centimetres [82]. Thus, the ability to detect lesions of at least 1 cm in diameter should prove to be adequate to both detect and monitor DTI.

In order to investigate the effect of lesion depth on the detection sensitivity, measured strain ratios for circular lesions with a diameter of 2.5 cm located at various depths were interrogated with a 4 MHz probing frequency, and strained

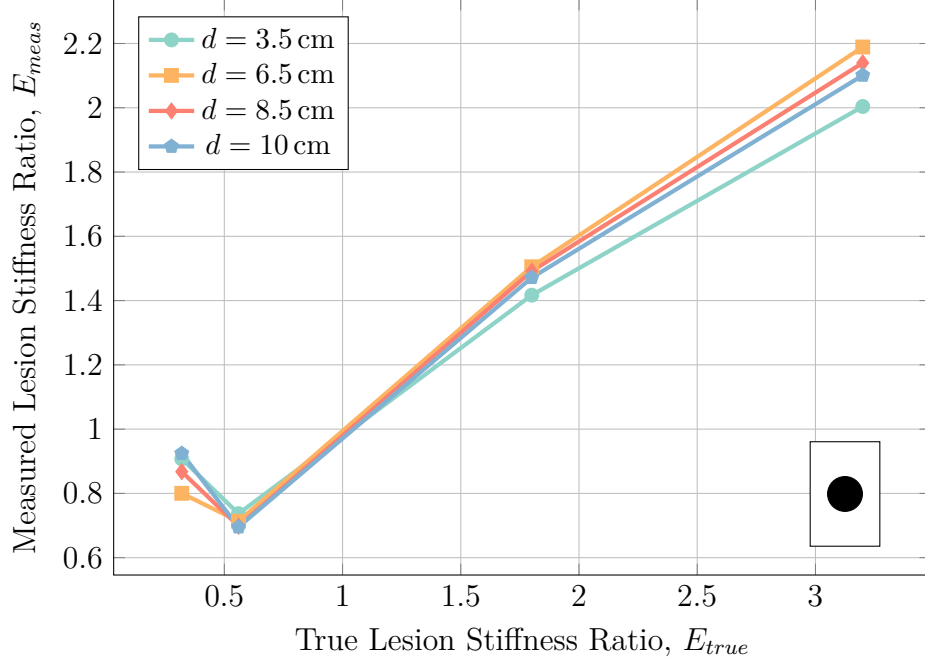


Fig. 3.9: Lesion depth characterization at a lesion diameter of 2.5 cm with a 4 MHz ultrasound probing frequency generally showing general independence of detection sensitivity on lesion depth in the tissue.

by 5 %. The results of this investigation are seen in Fig. 3.9.

In Fig. 3.9, it can be seen that there was little interplay between detection sensitivity and measured strain ratios at the various depths examined for all but the case for very soft (mushy) lesions (with a stiffness ratio of 0.32). At such low stiffness ratios, the excessive tissue deformation interrupts the tissue strain estimation algorithm's ability to adequately track the induced displacements in the lesion.

Since the strain field caused by compressive forces near an extremely rigid structure embedded within a relatively soft domain will be significantly heterogeneous, the effect of lesion altitude above the underlying stiff bone was examined with the hypothesis that if the lesion were too close to the hard bone, it would be masked by the strain field caused by the bone's existence. A 2.5 cm diameter lesion was interrogated with a 4 MHz probing frequency and 5 % applied strain. The results of this characterization are given in Fig. 3.10.

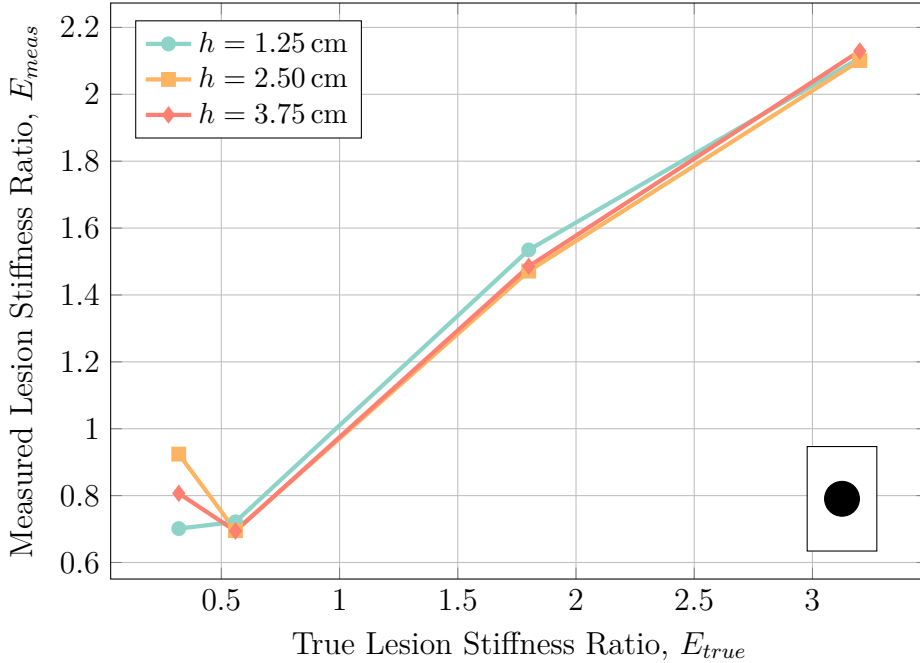


Fig. 3.10: Effect of lesion altitude above the underlying bone. Aside from erroneous results at very low lesion stiffness ratios, the effect is negligible.

In Fig. 3.10, it can be seen that the lesion altitude above the underlying bone had very little effect on the detection sensitivity. Although larger strain fields may be generated near the bone, it is hypothesized that the larger fields also extend larger and so affect healthy tissue to more or less the same degree as the forming lesion.

In order to characterize the effect of using alternate ultrasound probing frequencies, simulations were carried out on lesions using probing frequencies of 2 MHz, 4 MHz, and 8 MHz. The simulated lesions had a diameter of 2.5 cm, were located at a depth of 10 cm and we strain at 5 %. The results of this study are given in Fig. 3.11.

As can be seen from Fig. 3.11, there is very little effect on the detection sensitivity from the ultrasound probing frequency that was used, therefore an appropriate frequency should be chosen so as to reach the full depth of the bone-muscle interface at suspected DTI locations while retaining the best

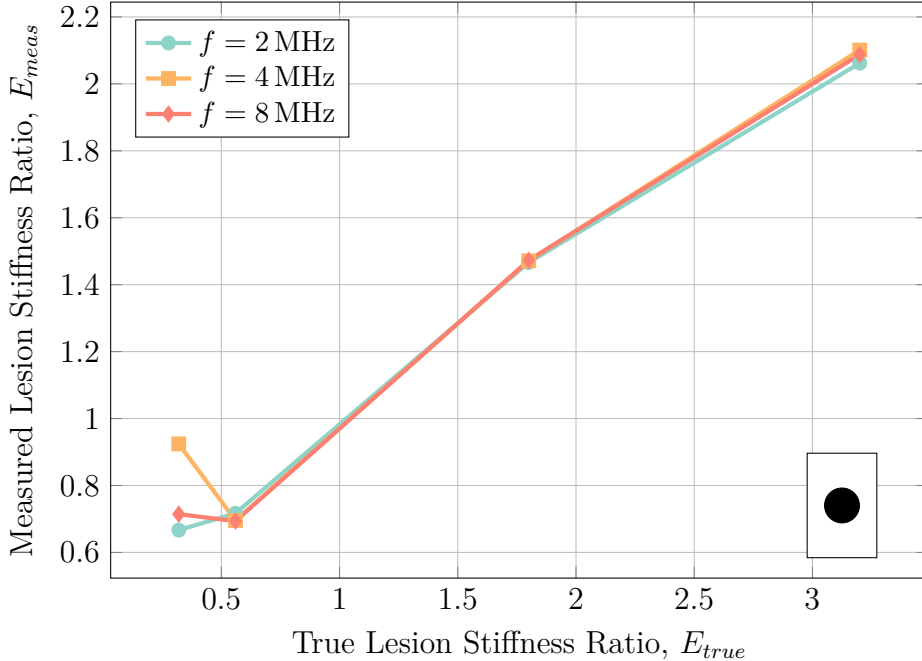


Fig. 3.11: Characterization of ultrasonic probing frequency on detection sensitivity. Apart from the requirement of using an ultrasonic frequency low enough to interrogate the desired tissue, probing frequency has negligible effect on the detection sensitivity.

image resolution.

As quasi-static ultrasound elastography is most likely to be performed via manual indentation where the exact magnitude of applied deformation is unknown, it is important to study the effect of applied strain magnitude on the detection sensitivity. Applied strains of 2.5 %, 5.0 %, and 10 % were investigated on a 2.5 cm diameter lesion at a depth of 10 cm using a probing frequency of 4 MHz; the results are given in Fig. 3.12.

While Fig. 3.12 shows a relatively constant detection sensitivity for compressive strains of 2.5 % and 5 %, compressive strains of 10 % generate significant measurement error for both very soft and very stiff lesions. Under large compressive strains, the tissue (either in the lesion as in the soft lesion case, or the surrounding tissue as in the stiff lesion case) deforms considerably which again interferes with the algorithm's ability to properly track the displacement

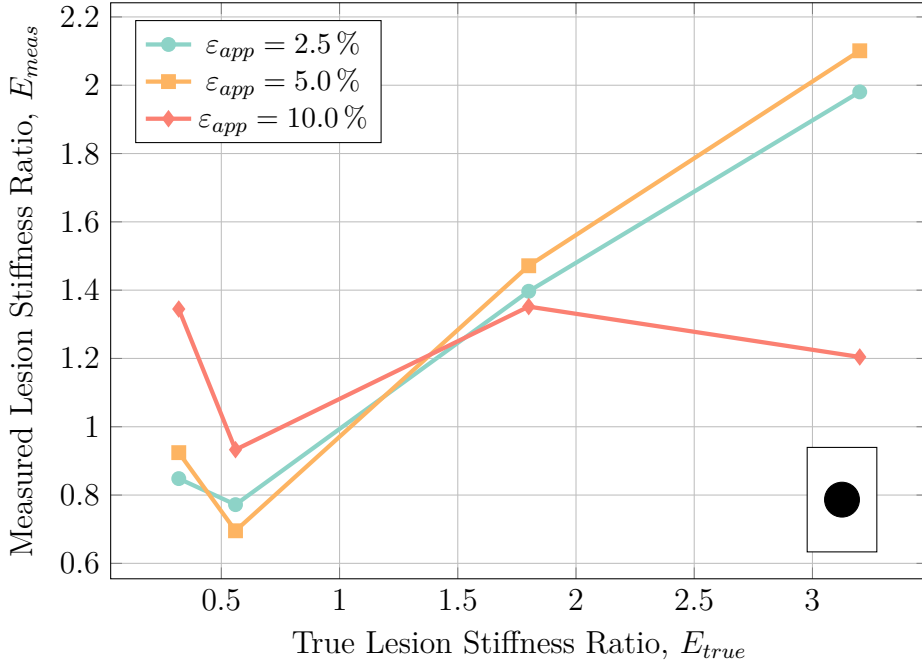


Fig. 3.12: Applied strain characterization plot for lesions with a diameter of 2.5 cm located at a depth of 10 cm interrogated at 4 MHz. There is little difference between 2.5 % and 5.0 % applied strain, while large-magnitude strains of 10 % generate significant error for both very soft and very stiff lesions.

of tissue. It should also be noted that applying overly large strains to an already forming deep tissue injury may cause additional unwarranted damage. Thus it is imperative that applied surface indentation be kept to reasonable bounds (2.5 % – 5 %, or 0.25 cm – 0.50 cm in 10 cm deep domains), not only for safety of the tissue but also for clarity of the diagnostic test.

To study the effect that closely spaced lesions will have on the detection sensitivity as well as how discernible the lesions will be from each other, the separation distance between two 1.0 cm diameter co-located lesions at a depth of 10 cm was examined using a 4 MHz probing frequency with 5 % applied strain magnitude. The results of this study are shown in 3.13.

While Fig. 3.13 shows that the separation distance between co-located lesions causes a negligible effect on the detection sensitivity, Fig. 3.14 shows regions of decreased strain above and below the centreline of the lesions. While

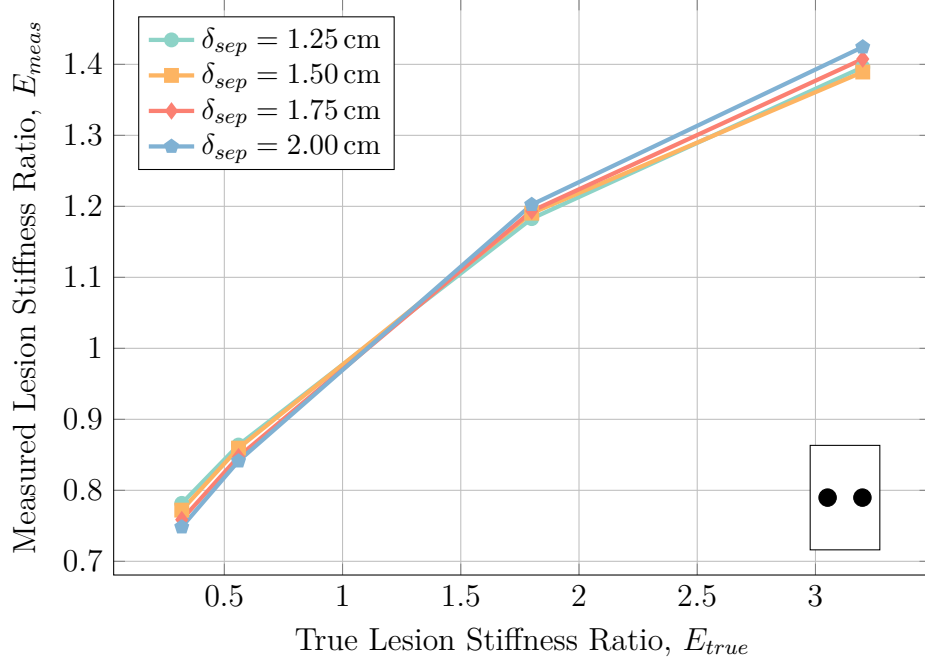


Fig. 3.13: Effect of lesion separation distance on two 1.0 cm diameter lesions co-located at a depth of 10 cm interrogated with a 4 MHz probe with 5 % applied strain. There is no negligible difference between separation distances on the detection sensitivity.

these regions had the same basal stiffness as the bulk tissue, the decreased strain pattern may obfuscate the true results by introducing “phantom lesions” which are not actually present but merely the result of the existing lesions.

While the simulations performed thus far assumed that lesions were perfect spheres with hard boundaries in order to isolate specific parameters of interest, this assumption may not always be accurate. Rather, due to the nature of injury formation, lesions may form gradual boundaries that “fade” from stiff or necrotic tissue to healthy tissue. To investigate the effect of this phenomenon on the detection sensitivity, lesions with “blurred boundaries” were investigated. Hard spherical lesions were blurred by convolving the lesion domain with a disc blurring kernel of varying radius. The results for this investigation on lesions with a diameter of 2.5 cm, at a depth of 10 cm and interrogated with a 4 MHz probing frequency with 5 % applied strain are given in Fig. 3.15.

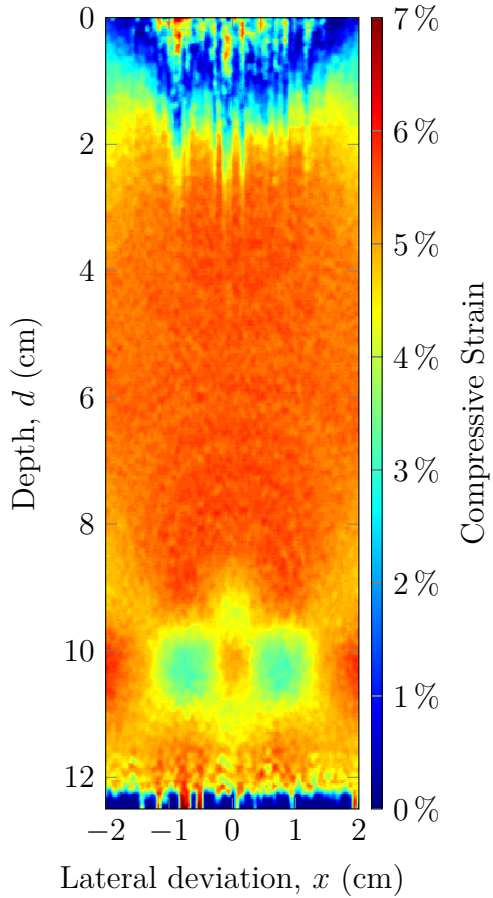


Fig. 3.14: Elastogram for two co-located lesions of 1.0 cm diameter at a depth of 10 cm interrogated using a 4 MHz probing frequency with 5 % applied strain. A pattern of decreased strain is present above and below the centerline between the two lesions while the lesions themselves are not affected by each other.

Fig. 3.15 shows that there is very little dependence on the lesion detection sensitivity for stiff lesions (lesions with a stiffness ratio ≥ 1.0). However, for soft lesions, the tissue strain estimation algorithm seems to over-estimate the stiffness of the lesions.

Similar to how lesions may have “blurred boundaries” rather than hard ones, so too may lesion composition not be homogeneous. In order to study the effect of heterogeneous regions of injured tissue, the detection sensitivity of a set of numerous small lesions located within close proximity to each other so as to form a large, heterogeneous area of diseased tissue was examined. Fig.

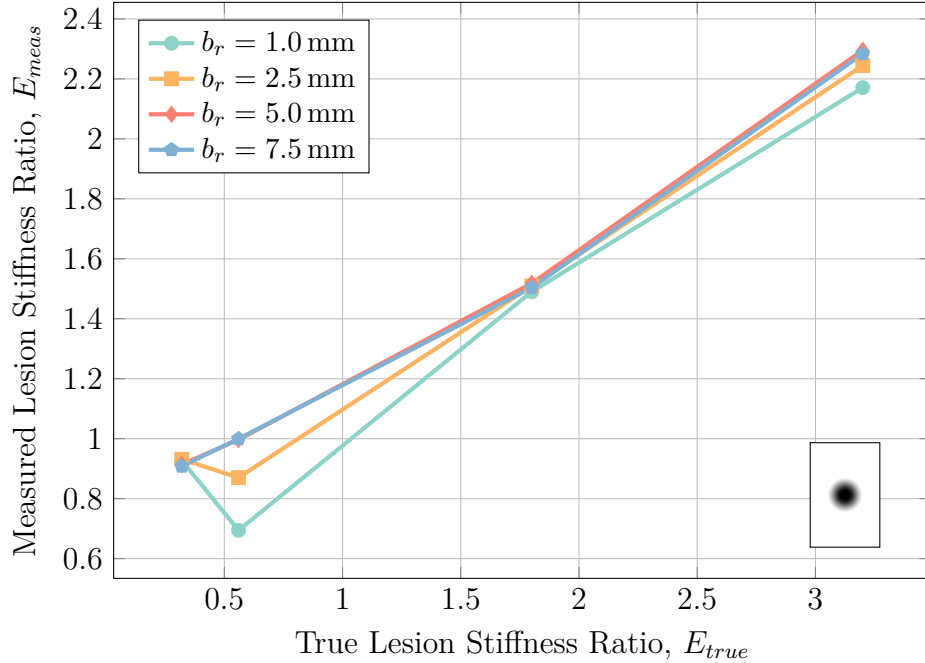


Fig. 3.15: Characterization of the effect of lesion blur radius on lesion detection sensitivity for a 2.5 cm diameter lesion at a depth of 10 cm using a probing frequency of 4 MHz and applied strain of 5 %. While there is negligible effect of the blur radius on stiff lesions, the strain ratio for soft lesions is considerably over-estimated.

3.16 shows the results for this model for varying numbers of 2 mm diameter lesions in a 2.5 cm diameter circle located at a depth of 10 cm with a probing frequency of 4 MHz and 5 % applied strain. Fig. 3.18 further explores this model by investigating the case where there are 30 small lesions per square cm with individual lesions ranging in diameter from 0.5 mm to 1.5 mm.

The characterization plot in Fig. 3.16 for small lesion density is less linear than other characterization plots, with lesion density having a significant effect on the detection sensitivity. Specifically, for low lesion densities, the detection sensitivity is much lower than for high lesion densities. However, this observation is warranted after examination of the elastogram produced from these results, given in Fig. 3.17, which shows how the small lesions are not individually detected but rather the entire region is detected as one large lesion. Since the average stiffness ratio over this region is lesser than the stiffness ratio of

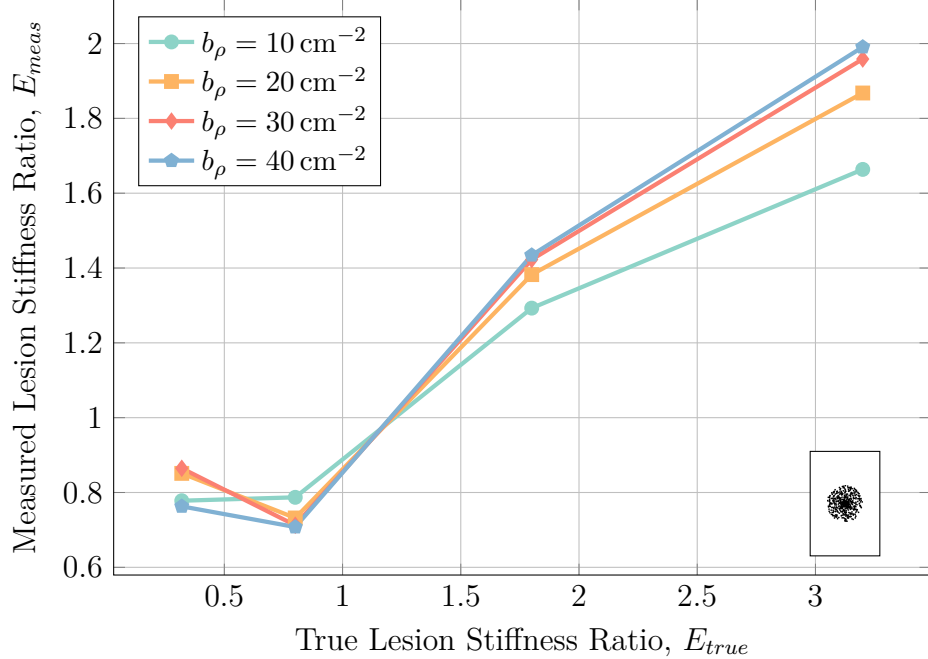


Fig. 3.16: Characterization of lesion density for a group of numerous smaller 2 mm diameter lesions comprising a large area with a diameter of 2.5 cm at a depth of 10 cm interrogated with a 4 MHz probing frequency and 5 % applied strain. Detection sensitivity decreases with decreasing lesion density, as expected.

individual lesions, it makes sense that the “measured” strain ratio will be less than expected.

Similar to the results shown in Fig. 3.16, changing the size of the individual small lesions does have an effect on the measured strain. In this case, when individual lesions are small, the total area occupied by lesions is lesser which results in a lesser average tissue stiffness over the grouped lesion region.

Note that although the elastography algorithm was able to detect the larger lesion-filled regions in these simulations, it was completely unable to discern the individual lesions comprising those regions. This is not surprising due to both the generated strain fields in the healthy tissue throughout the larger lesion area as well as the results presented in Fig. 3.8 showing poor detection sensitivity for lesions with diameters $\leq 1 \text{ cm}$ while the individual lesions in this simulation had diameters of the scale of 0.5 mm – 1.5 mm.

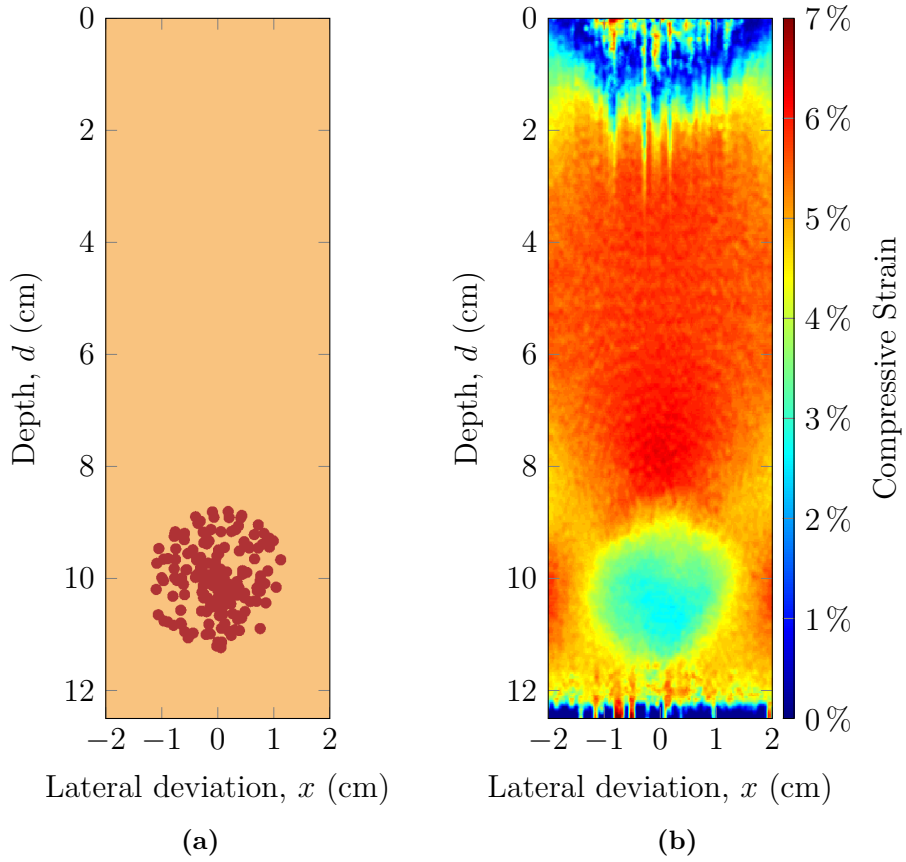


Fig. 3.17: Stiffness map (a) and corresponding elastogram (b) for a group of small lesions with a density of 10 lesions per cm^2 grouped in a 2.5 cm diameter circle at a depth of 10 cm interrogated with a 4 MHz probing frequency and 5 % applied strain. In (a), white regions are regular tissue while black regions are the small lesions. In the elastogram, individual lesions do not stand out, rather the entire region of lesions appears as one large region of unhealthy tissue.

Finally, in order to place these results within the context of a likely real scenario in humans, a more complicated model utilizing an MRI-acquired lesion and slides from the Visible Human Project [93] was developed. Specifically, lesion geometry was taken from a real deep tissue injury in a pig model imaged using T_2^* -weighted MRI. The human geometry was taken from a transverse plane slice across the left ischial tuberosity such that the lesion was placed immediately superficial to the boney prominence. For this model, the overall lesion width and lesion depth were examined with results shown in Figs. 3.19

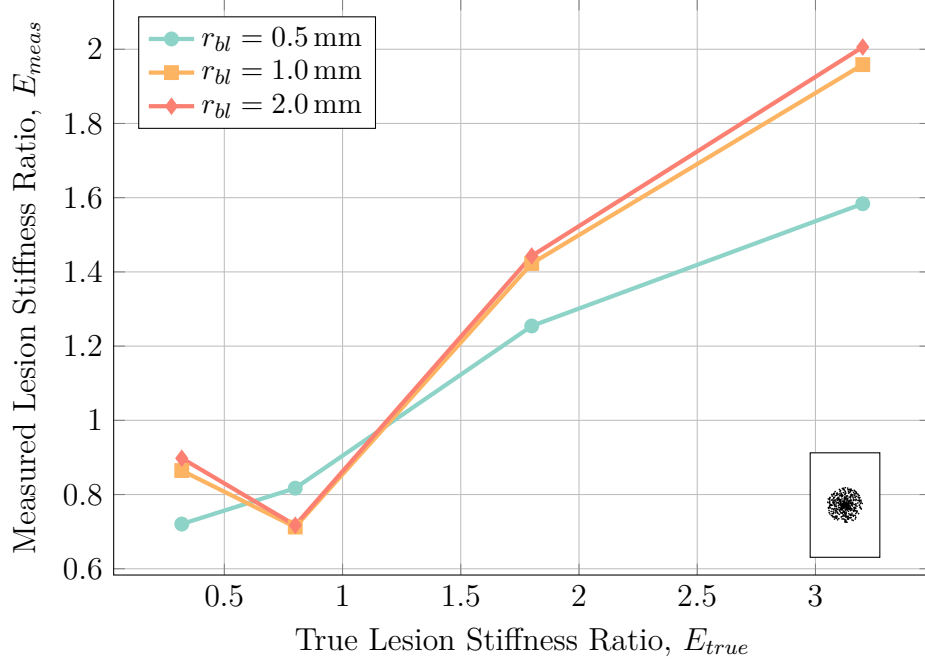


Fig. 3.18: Characterization of lesion radius for a group of numerous smaller lesions with a density of 30 lesions per cm^2 comprising a large area with a diameter of 2.5 cm at a depth of 10 cm interrogated with a 4 MHz probing frequency and 5% applied strain. Detection sensitivity decreases with decreasing individual lesion size, as expected.

and 3.21 respectively.

In Fig. 3.19, it is clear to see than small lesions (with a diameter $\leq 1.0\text{ cm}$) are almost impossible to adequately detect (although larger lesions will be adequately detectable). It is hypothesized that this phenomenon is due to the excessive strain apparent above the boney prominence that is seen in the resultant elastogram given in Fig. 3.20 such that the lesion is “washed out” by the strain field developed by the relatively stiff bone nearby.

In Fig. 3.21, there is little to no dependence of the detection sensitivity on the lesion depth in the Visible Human-MRI model with all depth curves displaying the same profile. However, deeper lesions (lesions closer to the bony prominence) have stiffnesses that are over-estimated with respect to their superficial counterparts. This is hypothesized to be due to the increased strain field present in all of the soft tissue located immediately superior to the bony

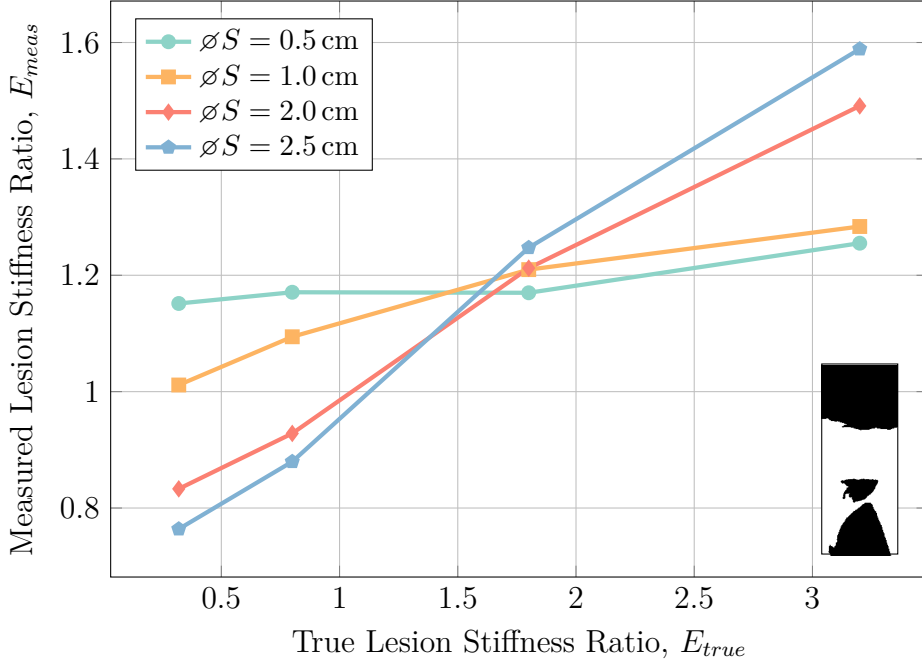


Fig. 3.19: Characterization of lesion width in a Visible Human-MRI model for lesions at a depth of 7.25 cm interrogated with a 4 MHz probing frequency with 5% applied strain. Small lesions (with a width $\leq 1.0 \text{ cm}$) are severely misrepresented and portray general over-estimation of lesion stiffness larger lesions.

prominence, but should not pose a serious problem for imaging lesions of this nature.

3.3.4 Physical Phantom Validation

In order to ensure that the models presented here represented physical realities, a small subset of the cases studied were modelled in a physical phantom, specifically for three lesions with stiffness ratios of 0.56, 1.80, and 3.20 with a diameter of 2.0 cm and at a depth of 3.5 cm, interrogated at 8 MHz with approximately 5% applied strain. The results of this study are summarized in Fig. 3.22.

As can be seen in Fig. 3.22, a relatively simple (although inexact) relationship between simulated and experimental measured strain ratios exists. It must be noted that the finite-element simulations of b-mode image formation

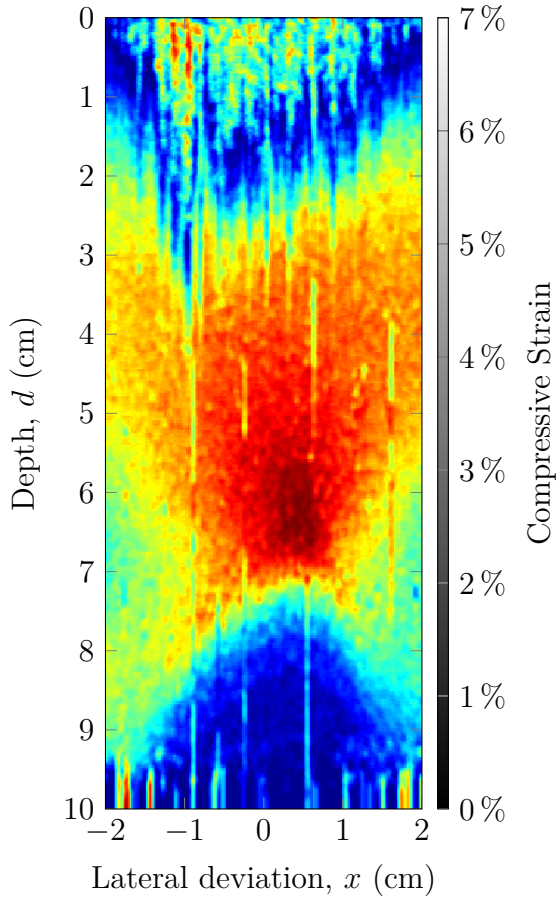


Fig. 3.20: Elastogram for a 0.5 cm wide lesion embedded in the Visible Human-MRI model domain at a depth of 7.25 cm interrogated at 4 MHz with an applied strain of 2.5 %. The lesion is not visible in the resultant elastogram.

and tissue deformation presented here are idealizations of reality and idealization errors such as the ultrasound pulse profile and plane-strain assumption no doubt contributed to the difference seen in Fig. 3.22.

It must be noted that in order to acquire quasi-static elastography results in the physical phantom, the ultrasound transducer was required to be manually manipulated to cause indentation in the phantom, as the technique would most likely be performed in a clinical setting. This was found to be problematic as the ultrasound transducer was difficult to maintain perfectly perpendicular and in-plane during the compression (largely due to the necessity of using coupling ultrasonic gel). This difficulty suggests that acoustic radiation force impulse

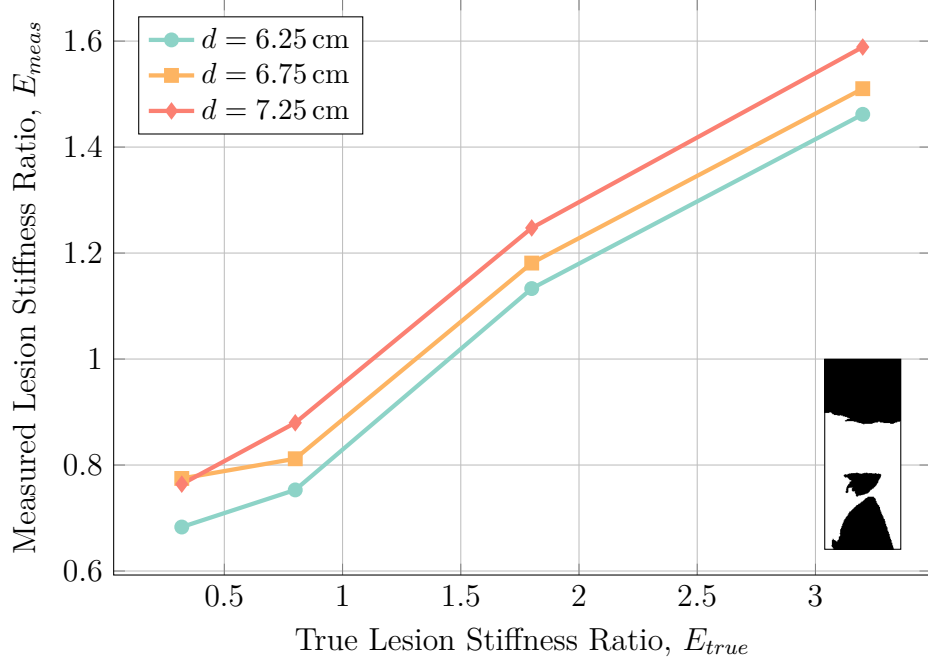


Fig. 3.21: Characterization of lesion depth in a Visible Human-MRI model for lesions with a width of 2.5cm interrogated with a 4MHz probing frequency and 5% applied strain. Deeper lesions (closer to the bony prominence) are have slightly over-estimated lesion stiffness ratios as opposed to more superficial lesions while detection sensitivity is not affected by lesion depth.

(ARFI) elastography would be a more appropriate method to acquire DTI elastograms. ARFI elastography works on the same principles as quasi-static elastography with the exception that tissue deformation is caused by localized large-amplitude acoustic waves generated by the transducer such that human factors play a far less substantial role in image acquisition.

3.4 Conclusion

With this work, we presented a numerical characterization of the use of quasi-static ultrasound elastography for the early detection of deep tissue injuries (DTI). There is a real clinical need for an objective tool that is capable of detecting the formation and progression of DTI in human subjects as these wounds are generally not visible from the surface of the skin until they have

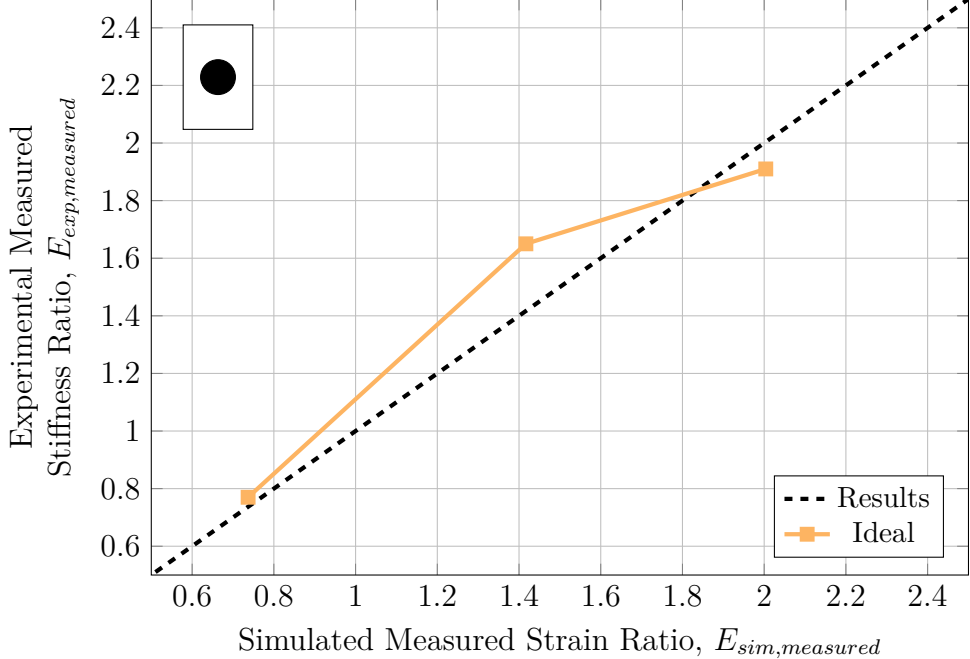


Fig. 3.22: Relation between simulated measured strain ratios and experimental measured strain ratios for a lesion at a depth of 3.5 cm and diameter of 2.0 cm showing general agreement between simulated and experimental cases. Idealization errors are the most likely the cause of the differences seen between simulated and experimental cases.

broken through and already caused substantial damage.

Through our numerical characterization, quasi-static ultrasound elastography was found to be an effective tool for detecting and monitoring DTI in theoretical simulations. Overall, detection sensitivity was less than expected. Small lesions (with diameters ≤ 1.0 cm) were more difficult to differentiate due to the low lesion detection sensitivity. While lesion depth, altitude above the underlying bone, and probing frequency did not have significant effect on the lesion detection sensitivity, it was found that applying high levels of compressive strain (10 %) introduced severe error for both very soft and very stiff lesions, thus it is recommended that diagnosticians only apply moderate ($\leq 5\%$) compressive strain when interrogating potential lesions. Larger strains may alternately be induced by slowly palpating the tissue with very minor strains frame-by-frame and cumulating the displacement fields across

these smaller palpations. Care must be used when palpating the tissue, lest “vigorous” palpations cause harm to the already sensitive injury. In the more complicated model of co-located lesions, while the separation distance between adjacent lesions did not affect the detection sensitivity, the placing of adjacent lesions generated “phantom” lesion regions with altered strain that may appear to be diseased tissue when they are in fact healthy. In a model lesion with gradual blurred boundaries, the effect of blur radius only affected the detection sensitivity and ability to differentiate soft lesions. Specifically, soft lesions with large blur radii became nearly impossible to differentiate as these lesions all showed a measured lesion stiffness ratio of approximately 1 which would show up as regular, healthy tissue. In the case of numerous clustered small lesions, both decreased lesion density and decreased individual lesion size caused a decrease in lesion detection sensitivity, likely due to the averaging effect of healthy tissue and diseased tissue in near proximity. Finally, in the Visible Human-MRI acquired lesion model, lesions with widths ≤ 1.0 cm are nearly impossible to differentiate as they are hidden by the strain field generated by the bony prominence. Lesion depth did not have an effect on the detection sensitivity, though deeper lesions (lesions which were closer to the bony prominence) had overestimated stiffnesses with respect to their more superficial counterparts.

Although the studies presented here resulted in less-than-ideal detection sensitivities, the technique was still able to pick out lesions from the surrounding soft (and hard) tissue. Work done by Solis et al. [82] has shown that untreated DTI are multiple centimeters in size, while work done by Gefen et al. [5] has shown that deep tissue injuries exhibit 1.8-fold to 3.3-fold mechanical stiffening. The work presented here has shown that quasi-static ultrasound elastography is adequate at detecting deep tissue injury lesions in these ranges

of parameters and will thus be adequate to detect and monitor progress DTI. However, without further real-world experimentation on the exact nature of newly-forming DTI, the detection sensitivity required to detect newly-forming DTI is indeterminate.

A subset of the results found through simulation were compared with similar experiments done using a tissue mimicking phantom model. The experimental results using the phantom model generally agreed with those found from simulation cases. It was also noted that the manual skin indentation technique involved with quasi-static ultrasound elastography proved to be difficult to produce reliable images. This difficulty suggests that an alternate method of performing ultrasound elastography may be preferable to quasi-static ultrasound elastography with manual indentation. Acoustic radiation force impulse (ARFI) elastography may be a more appropriate method to acquire DTI elastograms as although ARFI elastography works on the same principles as quasi-static elastography, the difference lays in the fact that tissue deformation is caused by localized large-amplitude acoustic waves generated by the transducer. This means that human factors play a far less substantial role in image acquisition and would likely improve repeatability and inter-operator reliability. Nevertheless, the work done here to characterize the use of quasi-static ultrasound elastography is an important step along the path of generating a useful clinical tool for detecting formative and monitoring progressive deep tissue injuries.

Chapter 4

Numerical Characterization of Acoustic Radiation Force Impulse Imaging

4.1 Introduction

4.2 Methods

4.2.1 Numerical Model

Governing Equations

The governing equations used for this model were the set of coupled first-order partial differential equations 4.1. These equations are the first-order equivalents of 4.2 taking into account acoustic absorption, tissue heterogeneities, and acoustic wave non-linearities [102].

$$\frac{\partial \mathbf{u}}{\partial t} = -\frac{1}{\rho_0} p \quad (4.1a)$$

$$\frac{\partial p}{\partial t} = -(2\rho + \rho_0) \nabla \cdot \mathbf{u} - \mathbf{u} \cdot \nabla \rho_0 \quad (4.1b)$$

$$p = c_0^2 \left(\rho + \mathbf{d} \cdot \nabla \rho_0 + \frac{B}{2A} \frac{\rho^2}{\rho_0} - L\rho \right) \quad (4.1c)$$

$$\nabla^2 p - \frac{1}{c_0^2} \frac{\partial^2 p}{\partial t^2} = 0 \quad (4.2)$$

Boundary and Initial Conditions

4.3 Results

Chapter 5

Numerical Characterization of Shear Wave Speed Quantification

Chapter 6

Conclusion

6.1 Clinical Need for DTI Detection

6.2 USE Provides Potential Diagnosis Capability

6.3 Future Work

6.3.1 Animal Studies?

6.3.2 Human Studies?

References

- [1] R. M. Allman, P. S. Goode, M. M. Patrick, N. Burst, and A. A. Bartolucci, “Pressure ulcer risk factors among hospitalized patients with activity limitation.” *JAMA : the journal of the American Medical Association*, vol. 273, no. 11, pp. 865–870, Mar. 15, 1995, ISSN: 0098-7484. [Online]. Available: <http://view.ncbi.nlm.nih.gov/pubmed/7869557>.
- [2] C. A. Salzberg, D. W. Byrne, C. G. Cayten, P. van Niewerburgh, J. G. Murphy, and M. Viehbeck, “A new pressure ulcer risk assessment scale for individuals with spinal cord injury.,” *American journal of physical medicine & rehabilitation / Association of Academic Physiatrists*, vol. 75, no. 2, pp. 96–104, 1996, ISSN: 0894-9115. [Online]. Available: <http://view.ncbi.nlm.nih.gov/pubmed/8630201>.
- [3] N. Kanno, T. Nakamura, M. Yamanaka, K. Kouda, T. Nakamura, and F. Tajima, “Low-echoic lesions underneath the skin in subjects with spinal-cord injury.,” *Spinal cord*, vol. 47, no. 3, pp. 225–229, Mar. 2009, ISSN: 1362-4393. DOI: 10 . 1038 / sc . 2008 . 101. [Online]. Available: <http://dx.doi.org/10.1038/sc.2008.101>.
- [4] A. Stekelenburg, D. Gawlitta, D. L. Bader, and C. W. Oomens, “Deep tissue injury: how deep is our understanding?” *Archives of physical medicine and rehabilitation*, vol. 89, no. 7, pp. 1410–1413, Jul. 2008,

- ISSN: 1532-821X. DOI: 10.1016/j.apmr.2008.01.012. [Online]. Available: <http://dx.doi.org/10.1016/j.apmr.2008.01.012>.
- [5] A. Gefen, N. Gefen, E. Linder-Ganz, and S. S. Margulies, “In vivo muscle stiffening under bone compression promotes deep pressure sores.,” *Journal of biomechanical engineering*, vol. 127, no. 3, pp. 512–524, Jun. 2005, ISSN: 0148-0731. [Online]. Available: <http://view.ncbi.nlm.nih.gov/pubmed/16060358>.
- [6] S. Loerakker, E. Manders, G. J. Strijkers, K. Nicolay, F. P. Baaijens, D. L. Bader, and C. W. Oomens, “The effects of deformation, ischemia, and reperfusion on the development of muscle damage during prolonged loading.,” *Journal of applied physiology (Bethesda, Md. : 1985)*, vol. 111, no. 4, pp. 1168–1177, Oct. 14, 2011, ISSN: 1522-1601. DOI: 10.1152/japplphysiol.00389.2011. [Online]. Available: <http://dx.doi.org/10.1152/japplphysiol.00389.2011>.
- [7] J. Black, M. M. M. Baharestani, J. Cuddigan, B. Dorner, L. Edsberg, D. Langemo, M. E. E. Posthauer, C. Ratliff, G. Taler, and National Pressure Ulcer Advisory Panel, “National pressure ulcer advisory panel’s updated pressure ulcer staging system.,” *Advances in skin & wound care*, vol. 20, no. 5, pp. 269–274, May 2007, ISSN: 1527-7941. DOI: 10.1097/01.asw.0000269314.23015.e9. [Online]. Available: <http://dx.doi.org/10.1097/01.asw.0000269314.23015.e9>.
- [8] C. V. Bouten, C. W. Oomens, F. P. Baaijens, and D. L. Bader, “The etiology of pressure ulcers: skin deep or muscle bound?” *Archives of physical medicine and rehabilitation*, vol. 84, no. 4, pp. 616–619, Apr. 2003, ISSN: 0003-9993. DOI: 10.1053/apmr.2003.50038. [Online]. Available: <http://dx.doi.org/10.1053/apmr.2003.50038>.

- [9] C. W. Oomens, S. Loerakker, and D. L. Bader, “The importance of internal strain as opposed to interface pressure in the prevention of pressure related deep tissue injury.,” *Journal of tissue viability*, vol. 19, no. 2, pp. 35–42, May 2010, ISSN: 0965-206X. DOI: 10.1016/j.jtv.2009.11.002. [Online]. Available: <http://dx.doi.org/10.1016/j.jtv.2009.11.002>.
- [10] A. Stekelenburg, C. W. Oomens, G. J. Strijkers, K. Nicolay, and D. L. Bader, “Compression-induced deep tissue injury examined with magnetic resonance imaging and histology.,” *Journal of applied physiology (Bethesda, Md. : 1985)*, vol. 100, no. 6, pp. 1946–1954, Jun. 2006, ISSN: 8750-7587. DOI: 10.1152/japplphysiol.00889.2005. [Online]. Available: <http://dx.doi.org/10.1152/japplphysiol.00889.2005>.
- [11] N. Aoi, K. Yoshimura, T. Kadono, G. Nakagami, S. Iizuka, T. Higashino, J. Araki, I. Koshima, and H. Sanada, “Ultrasound assessment of deep tissue injury in pressure ulcers: possible prediction of pressure ulcer progression.,” *Plastic and reconstructive surgery*, vol. 124, no. 2, pp. 540–550, Aug. 2009, ISSN: 1529-4242. DOI: 10.1097/prs.0b013e3181addb33. [Online]. Available: <http://dx.doi.org/10.1097/prs.0b013e3181addb33>.
- [12] M. Tanter, J. Bercoff, A. Athanasiou, T. Deffieux, J.-L. L. Gennisson, G. Montaldo, M. Muller, A. Tardivon, and M. Fink, “Quantitative assessment of breast lesion viscoelasticity: initial clinical results using supersonic shear imaging.,” *Ultrasound in medicine & biology*, vol. 34, no. 9, pp. 1373–1386, Sep. 2008, ISSN: 0301-5629. DOI: 10.1016/j.ultrasmedbio.2008.02.002. [Online]. Available: <http://dx.doi.org/10.1016/j.ultrasmedbio.2008.02.002>.

- [13] K. König, U. Scheipers, A. Pesavento, A. Lorenz, H. Ermert, and T. Senge, “Initial experiences with real-time elastography guided biopsies of the prostate.,” *The Journal of urology*, vol. 174, no. 1, pp. 115–117, Jul. 2005, ISSN: 0022-5347. DOI: 10.1097/01.ju.0000162043.72294.4a. [Online]. Available: <http://dx.doi.org/10.1097/01.ju.0000162043.72294.4a>.
- [14] L. Sandrin, B. Fourquet, J.-M. M. Hasquenoph, S. Yon, C. Fournier, F. Mal, C. Christidis, M. Ziol, B. Poulet, F. Kazemi, M. Beaugrand, and R. Palau, “Transient elastography: a new noninvasive method for assessment of hepatic fibrosis.,” *Ultrasound in medicine & biology*, vol. 29, no. 12, pp. 1705–1713, Dec. 2003, ISSN: 0301-5629. [Online]. Available: <http://view.ncbi.nlm.nih.gov/pubmed/14698338>.
- [15] E. Linder-Ganz and A. Gefen, “Mechanical compression-induced pressure sores in rat hindlimb: muscle stiffness, histology, and computational models.,” *Journal of applied physiology (Bethesda, Md. : 1985)*, vol. 96, no. 6, pp. 2034–2049, Jun. 2004, ISSN: 8750-7587. DOI: 10.1152/japplphysiol.00888.2003. [Online]. Available: <http://dx.doi.org/10.1152/japplphysiol.00888.2003>.
- [16] L. R. Solis, A. B. Liggins, P. Seres, R. R. Uwiera, N. R. Poppe, E. Pehowich, R. B. Thompson, and V. K. Mushahwar, “Distribution of internal strains around bony prominences in pigs.,” *Annals of biomedical engineering*, pp. 1–19, Mar. 8, 2012, ISSN: 1521-6047. DOI: 10.1007/s10439-012-0539-y. [Online]. Available: <http://dx.doi.org/10.1007/s10439-012-0539-y>.
- [17] A. Gefen, “Deep tissue injury from a bioengineering point of view.,” *Ostomy/wound management*, vol. 55, no. 4, pp. 26–36, Apr. 2009, ISSN:

- 0889-5899. [Online]. Available: <http://view.ncbi.nlm.nih.gov/pubmed/19387094>.
- [18] J.-F. F. Deprez, E. Brusseau, J. Fromageau, G. Cloutier, and O. Basset, “On the potential of ultrasound elastography for pressure ulcer early detection.,” *Medical physics*, vol. 38, no. 4, pp. 1943–1950, Apr. 2011, ISSN: 0094-2405. [Online]. Available: <http://view.ncbi.nlm.nih.gov/pubmed/21626927>.
- [19] K. Beckrich and S. A. Aronovitch, “Hospital-acquired pressure ulcers: a comparison of costs in medical vs. surgical patients.,” *Nursing economic\$*, vol. 17, no. 5, pp. 263–271, 1999, ISSN: 0746-1739. [Online]. Available: <http://view.ncbi.nlm.nih.gov/pubmed/10711175>.
- [20] C. Russo, C. Steiner, and W. Spector, “Hospitalizations related to pressure ulcers among adults 18 years and older, 2006: statistical brief no. 64.,” *Agency for Health Care Policy and Research (US)*, Dec. 2008. [Online]. Available: <http://www.ncbi.nlm.nih.gov/sites/entrez?Db=pubmed%5C%5C#38;Cmd>ShowDetailView%5C%5C#38;TermToSearch=21595131>.
- [21] J. M. Zanca, D. M. Brienza, D. Berlowitz, R. G. Bennett, C. H. Lyder, and National Pressure Ulcer Advisory Panel, “Pressure ulcer research funding in america: creation and analysis of an on-line database.,” *Advances in skin & wound care*, vol. 16, no. 4, pp. 190–197, 2003, ISSN: 1527-7941. [Online]. Available: <http://view.ncbi.nlm.nih.gov/pubmed/12897675>.
- [22] D. K. Langemo, H. Melland, D. Hanson, B. Olson, and S. Hunter, “The lived experience of having a pressure ulcer: a qualitative analysis.,” *Advances in skin & wound care*, vol. 13, no. 5, pp. 225–235, 2000, ISSN:

- 1527-7941. [Online]. Available: <http://view.ncbi.nlm.nih.gov/pubmed/11075022>.
- [23] M. M. Baharestani, “The lived experience of wives caring for their frail, homebound, elderly husbands with pressure ulcers.,” *Advances in wound care : the journal for prevention and healing*, vol. 7, no. 3, May 1994, ISSN: 1076-2191. [Online]. Available: <http://view.ncbi.nlm.nih.gov/pubmed/7827738>.
- [24] M. C. C. de Freitas, A. B. F. B. Medeiros, M. V. C. V. Guedes, P. C. C. de Almeida, F. T. T. de Galiza, and J. d. M. d. e. . M. Nogueira, “[pressure ulcers in the elderly: analysis of prevalence and risk factors].,” *Revista gaúcha de enfermagem / EENFUFRGS*, vol. 32, no. 1, pp. 143–150, Mar. 2011, ISSN: 0102-6933. [Online]. Available: <http://view.ncbi.nlm.nih.gov/pubmed/21888215>.
- [25] S. A. Aronovitch, “Intraoperatively acquired pressure ulcer prevalence: a national study.,” *Journal of wound, ostomy, and continence nursing*, vol. 26, no. 3, pp. 130–136, May 1999, ISSN: 1071-5754. [Online]. Available: <http://view.ncbi.nlm.nih.gov/pubmed/10711122>.
- [26] E. Jaul, “Assessment and management of pressure ulcers in the elderly: current strategies.,” *Drugs & aging*, vol. 27, no. 4, pp. 311–325, Apr. 1, 2010, ISSN: 1170-229X. DOI: 10.2165/11318340-000000000-00000. [Online]. Available: <http://dx.doi.org/10.2165/11318340-000000000-00000>.
- [27] Z. B. Niazi, C. A. Salzberg, D. W. Byrne, and M. Viehbeck, “Recurrence of initial pressure ulcer in persons with spinal cord injuries.,” *Advances in wound care : the journal for prevention and healing*, vol. 10, no. 3,

- pp. 38–42, 1997, ISSN: 1076-2191. [Online]. Available: <http://view.ncbi.nlm.nih.gov/pubmed/9306777>.
- [28] S. L. Garber and D. H. Rintala, “Pressure ulcers in veterans with spinal cord injury: a retrospective study.,” *Journal of rehabilitation research and development*, vol. 40, no. 5, pp. 433–441, 2003, ISSN: 0748-7711. [Online]. Available: <http://view.ncbi.nlm.nih.gov/pubmed/15080228>.
- [29] C. Campbell and L. C. C. Parish, “The decubitus ulcer: facts and controversies.,” *Clinics in dermatology*, vol. 28, no. 5, pp. 527–532, Sep. 2010, ISSN: 1879-1131. DOI: 10.1016/j.clindermatol.2010.03.010. [Online]. Available: <http://dx.doi.org/10.1016/j.clindermatol.2010.03.010>.
- [30] J. M. Black, L. E. Edsberg, M. M. Baharestani, D. Langemo, M. Goldberg, L. McNichol, J. Cuddigan, and National Pressure Ulcer Advisory Panel, “Pressure ulcers: avoidable or unavoidable? results of the national pressure ulcer advisory panel consensus conference.,” *Ostomy/wound management*, vol. 57, no. 2, pp. 24–37, Feb. 2011, ISSN: 1943-2720. [Online]. Available: <http://view.ncbi.nlm.nih.gov/pubmed/21350270>.
- [31] J. Maklebust, “Pressure ulcers: the great insult.,” *The Nursing clinics of North America*, vol. 40, no. 2, pp. 365–389, Jun. 2005, ISSN: 0029-6465. DOI: 10.1016/j.cnur.2004.09.015. [Online]. Available: <http://dx.doi.org/10.1016/j.cnur.2004.09.015>.
- [32] L. Gunningberg and N. A. Stotts, “Tracking quality over time: what do pressure ulcer data show?” *International journal for quality in health care : journal of the International Society for Quality in Health Care / ISQua*, vol. 20, no. 4, pp. 246–253, Aug. 2008, ISSN: 1353-4505. DOI:

- 10.1093/intqhc/mzn009. [Online]. Available: <http://dx.doi.org/10.1093/intqhc/mzn009>.
- [33] C. T. Milne, D. Trigilia, T. L. Houle, S. Delong, and D. Rosenblum, “Reducing pressure ulcer prevalence rates in the long-term acute care setting.,” *Ostomy/wound management*, vol. 55, no. 4, pp. 50–59, Apr. 2009, ISSN: 0889-5899. [Online]. Available: <http://view.ncbi.nlm.nih.gov/pubmed/19387096>.
- [34] J. A. Witkowski and L. C. Parish, “Histopathology of the decubitus ulcer.,” *Journal of the American Academy of Dermatology*, vol. 6, no. 6, pp. 1014–1021, Jun. 1982, ISSN: 0190-9622. [Online]. Available: <http://view.ncbi.nlm.nih.gov/pubmed/7096663>.
- [35] S. M. Dinsdale, “Decubitus ulcers: role of pressure and friction in causation.,” *Archives of physical medicine and rehabilitation*, vol. 55, no. 4, pp. 147–152, Apr. 1974, ISSN: 0003-9993. [Online]. Available: <http://view.ncbi.nlm.nih.gov/pubmed/4595834>.
- [36] M. KOSIAK, “Etiology of decubitus ulcers.,” *Archives of physical medicine and rehabilitation*, vol. 42, pp. 19–29, Jan. 1961, ISSN: 0003-9993. [Online]. Available: <http://view.ncbi.nlm.nih.gov/pubmed/13753341>.
- [37] R. Labbe, T. Lindsay, and P. M. Walker, “The extent and distribution of skeletal muscle necrosis after graded periods of complete ischemia.,” *Journal of vascular surgery*, vol. 6, no. 2, pp. 152–157, Aug. 1987, ISSN: 0741-5214. DOI: 10.1067/mva.1987.avs0060152. [Online]. Available: <http://dx.doi.org/10.1067/mva.1987.avs0060152>.
- [38] P. E. Strock and G. Majno, “Microvascular changes in acutely ischemic rat muscle.,” *Surgery, gynecology & obstetrics*, vol. 129, no. 6, pp. 1213–

- 1224, Dec. 1969, ISSN: 0039-6087. [Online]. Available: <http://view.ncbi.nlm.nih.gov/pubmed/5353417>.
- [39] M. Bliss and B. Simini, “When are the seeds of postoperative pressure sores sown?. often during surgery.,” *BMJ (Clinical research ed.)*, vol. 319, no. 7214, pp. 863–864, Oct. 2, 1999, ISSN: 0959-8138. [Online]. Available: <http://www.ncbi.nlm.nih.gov/pmc/articles/PMC1116702/>.
- [40] K. Ytrehus, O. Reikerås, N. Huseby, and R. Myklebust, “Ultrastructure of reperfused skeletal muscle: the effect of oxygen radical scavenger enzymes.,” *International journal of microcirculation, clinical and experimental / sponsored by the European Society for Microcirculation*, vol. 15, no. 4, pp. 155–162, 1995, ISSN: 0167-6865. [Online]. Available: <http://view.ncbi.nlm.nih.gov/pubmed/8847175>.
- [41] F. W. Blaisdell, “The pathophysiology of skeletal muscle ischemia and the reperfusion syndrome: a review.,” *Cardiovascular surgery (London, England)*, vol. 10, no. 6, pp. 620–630, Dec. 2002, ISSN: 0967-2109. [Online]. Available: <http://view.ncbi.nlm.nih.gov/pubmed/12453699>.
- [42] S. Tsuji, S. Ichioka, N. Sekiya, and T. Nakatsuka, “Analysis of ischemia-reperfusion injury in a microcirculatory model of pressure ulcers.,” *Wound repair and regeneration*, vol. 13, no. 2, pp. 209–215, Mar. 2005, ISSN: 1067-1927. DOI: [10.1111/j.1067-1927.2005.130213.x](https://doi.org/10.1111/j.1067-1927.2005.130213.x). [Online]. Available: <http://dx.doi.org/10.1111/j.1067-1927.2005.130213.x>.
- [43] R. Salcido, J. C. Donofrio, S. B. Fisher, E. K. LeGrand, K. Dickey, J. M. Carney, R. Schosser, and R. Liang, “Histopathology of pressure ulcers as a result of sequential computer-controlled pressure sessions in a fuzzy

- rat model.,” *Advances in wound care : the journal for prevention and healing*, vol. 7, no. 5, Sep. 1994, ISSN: 1076-2191. [Online]. Available: <http://view.ncbi.nlm.nih.gov/pubmed/7889250>.
- [44] G. E. Miller and J. Seale, “Lymphatic clearance during compressive loading.,” *Lymphology*, vol. 14, no. 4, pp. 161–166, Dec. 1981, ISSN: 0024-7766. [Online]. Available: <http://view.ncbi.nlm.nih.gov/pubmed/7334832>.
- [45] T. A. Krouskop, N. P. Reddy, W. A. Spencer, and J. W. Secor, “Mechanisms of decubitus ulcer formation—an hypothesis.,” *Medical hypotheses*, vol. 4, no. 1, pp. 37–39, 1978, ISSN: 0306-9877. [Online]. Available: <http://view.ncbi.nlm.nih.gov/pubmed/634177>.
- [46] N. P. Reddy and G. V. Cochran, “Interstitial fluid flow as a factor in decubitus ulcer formation.,” *Journal of biomechanics*, vol. 14, no. 12, pp. 879–881, 1981, ISSN: 0021-9290. [Online]. Available: <http://view.ncbi.nlm.nih.gov/pubmed/7328094>.
- [47] B. Braden and N. Bergstrom, “A conceptual schema for the study of the etiology of pressure sores.,” *Rehabilitation nursing : the official journal of the Association of Rehabilitation Nurses*, vol. 12, no. 1, pp. 8–12, 1987, ISSN: 0278-4807. [Online]. Available: <http://view.ncbi.nlm.nih.gov/pubmed/3643620>.
- [48] A. S. Landsman, D. F. Meaney, R. S. Cargill, E. J. Macarak, and L. E. Thibault, “1995 william j. stickel gold award. high strain rate tissue deformation. a theory on the mechanical etiology of diabetic foot ulcerations.,” *Journal of the American Podiatric Medical Association*, vol. 85, no. 10, pp. 519–527, Oct. 1995, ISSN: 8750-7315. [Online]. Available: <http://view.ncbi.nlm.nih.gov/pubmed/7473083>.

- [49] C. V. Bouten, M. M. Knight, D. A. Lee, and D. L. Bade, “Compressive deformation and damage of muscle cell subpopulations in a model system.,” *Annals of biomedical engineering*, vol. 29, no. 2, pp. 153–163, Feb. 2001, ISSN: 0090-6964. [Online]. Available: <http://view.ncbi.nlm.nih.gov/pubmed/11284670>.
- [50] Y.-N. N. Wang, C. V. Bouten, D. A. Lee, and D. L. Bader, “Compression-induced damage in a muscle cell model in vitro.,” *Proceedings of the Institution of Mechanical Engineers. Part H, Journal of engineering in medicine*, vol. 219, no. 1, pp. 1–12, 2005, ISSN: 0954-4119. [Online]. Available: <http://view.ncbi.nlm.nih.gov/pubmed/15777052>.
- [51] K. K. Ceelen, A. Stekelenburg, S. Loerakker, G. J. Strijkers, D. L. Bader, K. Nicolay, F. P. Baaijens, and C. W. Oomens, “Compression-induced damage and internal tissue strains are related.,” *Journal of biomechanics*, vol. 41, no. 16, pp. 3399–3404, Dec. 5, 2008, ISSN: 0021-9290. DOI: 10.1016/j.jbiomech.2008.09.016. [Online]. Available: <http://dx.doi.org/10.1016/j.jbiomech.2008.09.016>.
- [52] E. Linder-Ganz, N. Shabshin, Y. Itzchak, Z. Yizhar, I. Siev-Ner, and A. Gefen, “Strains and stresses in sub-dermal tissues of the buttocks are greater in paraplegics than in healthy during sitting.,” *Journal of biomechanics*, vol. 41, no. 3, pp. 567–580, 2008, ISSN: 0021-9290. DOI: 10.1016/j.jbiomech.2007.10.011. [Online]. Available: <http://dx.doi.org/10.1016/j.jbiomech.2007.10.011>.
- [53] S. Portnoy, I. Siev-Ner, N. Shabshin, A. Kristal, Z. Yizhar, and A. Gefen, “Patient-specific analyses of deep tissue loads post transtibial amputation in residual limbs of multiple prosthetic users.,” *Journal of biomechanics*, vol. 42, no. 16, pp. 2686–2693, Dec. 11, 2009, ISSN: 1873-

2380. DOI: 10.1016/j.jbiomech.2009.08.019. [Online]. Available: <http://dx.doi.org/10.1016/j.jbiomech.2009.08.019>.
- [54] N. Slomka and A. Gefen, “Relationship between strain levels and permeability of the plasma membrane in statically stretched myoblasts.,” *Annals of biomedical engineering*, vol. 40, no. 3, pp. 606–618, Mar. 7, 2012, ISSN: 1573-9686. DOI: 10.1007/s10439-011-0423-1. [Online]. Available: <http://dx.doi.org/10.1007/s10439-011-0423-1>.
- [55] S. Loerakker, L. R. Solis, D. L. Bader, F. P. Baaijens, V. K. Mushahwar, and C. W. Oomens, “How does muscle stiffness affect the internal deformations within the soft tissue layers of the buttocks under constant loading?” *Computer methods in biomechanics and biomedical engineering*, vol. 16, no. 5, pp. 520–529, 2013, ISSN: 1476-8259. DOI: 10.1080/10255842.2011.627682. [Online]. Available: <http://dx.doi.org/10.1080/10255842.2011.627682>.
- [56] E. Linder-Ganz and A. Gefen, “Stress analyses coupled with damage laws to determine biomechanical risk factors for deep tissue injury during sitting.,” *Journal of biomechanical engineering*, vol. 131, no. 1, Jan. 2009, ISSN: 0148-0731. DOI: 10.1115/1.3005195. [Online]. Available: <http://dx.doi.org/10.1115/1.3005195>.
- [57] T. Nagel, S. Loerakker, and C. W. Oomens, “A theoretical model to study the effects of cellular stiffening on the damage evolution in deep tissue injury.,” *Computer methods in biomechanics and biomedical engineering*, vol. 12, no. 5, pp. 585–597, Oct. 2009, ISSN: 1476-8259. DOI: 10.1080/10255840902788603. [Online]. Available: <http://dx.doi.org/10.1080/10255840902788603>.

- [58] A. Gefen and E. Linder-Ganz, “[diffusion of ulcers in the diabetic foot is promoted by stiffening of plantar muscular tissue under excessive bone compression].,” *Der Orthopäde*, vol. 33, no. 9, pp. 999–1012, Sep. 2004, ISSN: 0085-4530. DOI: 10.1007/s00132-004-0701-9. [Online]. Available: <http://dx.doi.org/10.1007/s00132-004-0701-9>.
- [59] D. DiMaio and Vincent, “Rigor mortis,” in *Forensic Pathology, Second Edition (Practical Aspects of Criminal and Forensic Investigations)*, V. J. Geberth, Ed., 2nd ed. CRC Press, Jun. 28, 2001, pp. 26–28, ISBN: 084930072X. [Online]. Available: <http://www.amazon.com/exec/obidos/redirect?tag=citeulike07-20%5C&path=ASIN/084930072X>.
- [60] S. Portnoy, Z. Yizhar, N. Shabshin, Y. Itzchak, A. Kristal, Y. Dotan-Marom, I. Siev-Ner, and A. Gefen, “Internal mechanical conditions in the soft tissues of a residual limb of a trans-tibial amputee.,” *Journal of biomechanics*, vol. 41, no. 9, pp. 1897–1909, 2008, ISSN: 0021-9290. DOI: 10.1016/j.jbiomech.2008.03.035. [Online]. Available: <http://dx.doi.org/10.1016/j.jbiomech.2008.03.035>.
- [61] D. Norton, R. McLaren, and A. N. Exton-Smith, *An Investigation Of Geriatric Nursing Problems In Hospital*, 5. London, UK: Churchill Livingstone, Jul. 1975, vol. 77, pp. 317+. DOI: 10.1016/s0033-3506(63)80071-2. [Online]. Available: [http://dx.doi.org/10.1016/s0033-3506\(63\)80071-2](http://dx.doi.org/10.1016/s0033-3506(63)80071-2).
- [62] B. J. Braden and N. Bergstrom, “Predictive validity of the braden scale for pressure sore risk in a nursing home population.,” *Research in nursing & health*, vol. 17, no. 6, pp. 459–470, Dec. 1994, ISSN: 0160-

6891. [Online]. Available: <http://view.ncbi.nlm.nih.gov/pubmed/7972924>.
- [63] M. Lindgren, M. Unosson, A.-M. M. Krantz, and A.-C. C. Ek, “A risk assessment scale for the prediction of pressure sore development: reliability and validity.,” *Journal of advanced nursing*, vol. 38, no. 2, pp. 190–199, Apr. 2002, ISSN: 0309-2402. [Online]. Available: <http://view.ncbi.nlm.nih.gov/pubmed/11940132>.
- [64] I. Fromantin, M. C. Falcou, A. Baffie, C. Petot, R. Mazerat, C. Jaouen, L. Téot, and d. Rycke, “Inception and validation of a pressure ulcer risk scale in oncology.,” *Journal of wound care*, vol. 20, no. 7, Jul. 2011, ISSN: 0969-0700. [Online]. Available: <http://view.ncbi.nlm.nih.gov/pubmed/21841721>.
- [65] U. Källman and M. Lindgren, “Predictive validity of 4 risk assessment scales for prediction of pressure ulcer development in a hospital setting.,” *Advances in skin & wound care*, vol. 27, no. 2, pp. 70–76, Feb. 2014, ISSN: 1538-8654. DOI: 10.1097/01.asw.0000439059.72199.41. [Online]. Available: <http://dx.doi.org/10.1097/01.asw.0000439059.72199.41>.
- [66] Y. J. J. Lee, S. Park, J. Y. Y. Kim, C. G. G. Kim, and S. K. K. Cha, “[clinical nurses’ knowledge and visual differentiation ability in pressure ulcer classification system and incontinence-associated dermatitis].,” *Journal of Korean Academy of Nursing*, vol. 43, no. 4, pp. 526–535, Aug. 2013, ISSN: 2093-758X. DOI: 10.4040/jkan.2013.43.4.526. [Online]. Available: <http://dx.doi.org/10.4040/jkan.2013.43.4.526>.
- [67] J. M. Levine, E. A. Ayello, K. M. Zulkowski, and J. Fogel, “Pressure ulcer knowledge in medical residents: an opportunity for improvement.,”

- Advances in skin & wound care*, vol. 25, no. 3, pp. 115–117, Mar. 2012, ISSN: 1538-8654. DOI: 10.1097/01.asw.0000412908.43335.46. [Online]. Available: <http://dx.doi.org/10.1097/01.asw.0000412908.43335.46>.
- [68] E. Sloth and T. Karlsmark, “Evaluation of four non-invasive methods for examination and characterization of pressure ulcers.,” *Skin research and technology : official journal of International Society for Bioengineering and the Skin (ISBS) [and] International Society for Digital Imaging of Skin (ISDIS) [and] International Society for Skin Imaging (ISSI)*, vol. 14, no. 3, pp. 270–276, Aug. 2008, ISSN: 1600-0846. DOI: 10.1111/j.1600-0846.2008.00290.x. [Online]. Available: <http://dx.doi.org/10.1111/j.1600-0846.2008.00290.x>.
- [69] T. Higashino, G. Nakagami, T. Kadono, Y. Ogawa, S. Iizaka, H. Koyanagi, S. Sasaki, N. Haga, and H. Sanada, “Combination of thermographic and ultrasonographic assessments for early detection of deep tissue injury.,” *International wound journal*, Nov. 22, 2012, ISSN: 1742-481X. DOI: 10.1111/j.1742-481x.2012.01117.x. [Online]. Available: <http://dx.doi.org/10.1111/j.1742-481x.2012.01117.x>.
- [70] C. Gehin, E. Brusseau, R. Meffre, P. M. Schmitt, J. F. Deprez, and A. Dittmar, “Which techniques to improve the early detection and prevention of pressure ulcers?” *Conference proceedings : ... Annual International Conference of the IEEE Engineering in Medicine and Biology Society. IEEE Engineering in Medicine and Biology Society. Conference*, vol. 1, pp. 6057–6060, 2006, ISSN: 1557-170X. DOI: 10.1109/iembs.2006.259506. [Online]. Available: <http://dx.doi.org/10.1109/iembs.2006.259506>.

- [71] A. Gefen, K. J. Farid, and I. Shaywitz, “A review of deep tissue injury development, detection, and prevention: shear savvy.,” *Ostomy/wound management*, vol. 59, no. 2, pp. 26–35, Feb. 2013, ISSN: 1943-2720. [Online]. Available: <http://view.ncbi.nlm.nih.gov/pubmed/23388395>.
- [72] J.-F. F. Deprez, G. Cloutier, C. Schmitt, C. Gehin, A. Dittmar, O. Basset, and E. Brusseau, “3D ultrasound elastography for early detection of lesions. evaluation on a pressure ulcer mimicking phantom.,” *Conference proceedings : ... Annual International Conference of the IEEE Engineering in Medicine and Biology Society. IEEE Engineering in Medicine and Biology Society. Conference*, vol. 2007, pp. 79–82, 2007, ISSN: 1557-170X. DOI: 10.1109/embc.2007.4352227. [Online]. Available: <http://dx.doi.org/10.1109/embc.2007.4352227>.
- [73] R. Beetham, “Biochemical investigation of suspected rhabdomyolysis.,” *Annals of clinical biochemistry*, vol. 37 (Pt 5), pp. 581–587, Sep. 2000, ISSN: 0004-5632. [Online]. Available: <http://view.ncbi.nlm.nih.gov/pubmed/11026512>.
- [74] J. M. Sauret, G. Marinides, and G. K. Wang, “Rhabdomyolysis.,” *American family physician*, vol. 65, no. 5, pp. 907–912, Mar. 1, 2002, ISSN: 0002-838X. [Online]. Available: <http://view.ncbi.nlm.nih.gov/pubmed/11898964>.
- [75] W. H. Bagley, H. Yang, and K. H. Shah, “Rhabdomyolysis.,” *Internal and emergency medicine*, vol. 2, no. 3, pp. 210–218, Oct. 2007, ISSN: 1828-0447. DOI: 10.1007/s11739-007-0060-8. [Online]. Available: <http://dx.doi.org/10.1007/s11739-007-0060-8>.
- [76] K. Vanderwee, M. H. Grypdonck, D. De Bacquer, and T. Defloor, “Effectiveness of turning with unequal time intervals on the incidence of

- pressure ulcer lesions.,” *Journal of advanced nursing*, vol. 57, no. 1, pp. 59–68, Jan. 2007, ISSN: 0309-2402. DOI: 10.1111/j.1365-2648.2006.04060.x. [Online]. Available: <http://dx.doi.org/10.1111/j.1365-2648.2006.04060.x>.
- [77] S. E. Rich, D. Margolis, M. Shardell, W. G. Hawkes, R. R. Miller, S. Amr, and M. Baumgarten, “Frequent manual repositioning and incidence of pressure ulcers among bed-bound elderly hip fracture patients.,” *Wound repair and regeneration*, vol. 19, no. 1, pp. 10–18, 2011, ISSN: 1524-475X. DOI: 10.1111/j.1524-475x.2010.00644.x. [Online]. Available: <http://dx.doi.org/10.1111/j.1524-475x.2010.00644.x>.
- [78] T. A. Krouskop, P. S. Noble, J. Brown, and R. Marburger, “Factors affecting the pressure-distributing properties of foam mattress overlays.,” *Journal of rehabilitation research and development*, vol. 23, no. 3, pp. 33–39, Jul. 1986, ISSN: 0748-7711. [Online]. Available: <http://view.ncbi.nlm.nih.gov/pubmed/3772816>.
- [79] B. Pham, L. Teague, J. Mahoney, L. Goodman, M. Paulden, J. Poss, J. Li, L. Ieraci, S. Carcone, and M. Krahn, “Early prevention of pressure ulcers among elderly patients admitted through emergency departments: a cost-effectiveness analysis.,” *Annals of emergency medicine*, vol. 58, no. 5, Nov. 2011, ISSN: 1097-6760. DOI: 10.1016/j.annemergmed.2011.04.033. [Online]. Available: <http://dx.doi.org/10.1016/j.annemergmed.2011.04.033>.
- [80] L. Rafter, “Evaluation of patient outcomes: pressure ulcer prevention mattresses.,” *British journal of nursing (Mark Allen Publishing)*, vol.

- 20, no. 11, 2011, ISSN: 0966-0461. [Online]. Available: <http://view.ncbi.nlm.nih.gov/pubmed/21727848>.
- [81] S. Gyawali, L. Solis, S. L. L. Chong, C. Curtis, P. Seres, I. Kornelsen, R. Thompson, and V. K. Mushahwar, “Intermittent electrical stimulation redistributes pressure and promotes tissue oxygenation in loaded muscles of individuals with spinal cord injury.,” *Journal of applied physiology (Bethesda, Md. : 1985)*, vol. 110, no. 1, pp. 246–255, Jan. 2011, ISSN: 1522-1601. DOI: 10.1152/japplphysiol.00661.2010. [Online]. Available: <http://dx.doi.org/10.1152/japplphysiol.00661.2010>.
- [82] L. R. Solis, E. Twist, P. Seres, R. B. Thompson, and V. K. Mushahwar, “Prevention of deep tissue injury through muscle contractions induced by intermittent electrical stimulation after spinal cord injury in pigs.,” *Journal of applied physiology (Bethesda, Md. : 1985)*, vol. 114, no. 2, pp. 286–296, Jan. 15, 2013, ISSN: 1522-1601. DOI: 10.1152/japplphysiol.00257.2012. [Online]. Available: <http://dx.doi.org/10.1152/japplphysiol.00257.2012>.
- [83] N. Greer, N. A. Foman, R. MacDonald, J. Dorrian, P. Fitzgerald, I. Rutks, and T. J. Wilt, “Advanced wound care therapies for nonhealing diabetic, venous, and arterial ulcers: a systematic review.,” *Annals of internal medicine*, vol. 159, no. 8, pp. 532–542, Oct. 15, 2013, ISSN: 1539-3704. DOI: 10.7326/0003-4819-159-8-201310150-00006. [Online]. Available: <http://dx.doi.org/10.7326/0003-4819-159-8-201310150-00006>.
- [84] R. L. Longe, “Current concepts in clinical therapeutics: pressure sores.,” *Clinical pharmacy*, vol. 5, no. 8, pp. 669–681, Aug. 1986, ISSN: 0278-

2677. [Online]. Available: <http://view.ncbi.nlm.nih.gov/pubmed/3527529>.
- [85] H. Brem, D. M. Nierman, and J. E. Nelson, “Pressure ulcers in the chronically critically ill patient.,” *Critical care clinics*, vol. 18, no. 3, pp. 683–694, Jul. 2002, ISSN: 0749-0704. [Online]. Available: <http://view.ncbi.nlm.nih.gov/pubmed/12140919>.
- [86] B. Biglari, A. Büchler, T. Reitzel, T. Swing, H. J. Gerner, T. Ferbert, and A. Moghaddam, “A retrospective study on flap complications after pressure ulcer surgery in spinal cord-injured patients.,” *Spinal cord*, vol. 52, no. 1, pp. 80–83, Jan. 12, 2014, ISSN: 1476-5624. DOI: 10.1038/sc.2013.130. [Online]. Available: <http://dx.doi.org/10.1038/sc.2013.130>.
- [87] I. Bales and T. Duvendack, “Reaching for the moon: achieving zero pressure ulcer prevalence, an update.,” *Journal of wound care*, vol. 20, no. 8, Aug. 2011, ISSN: 0969-0700. [Online]. Available: <http://view.ncbi.nlm.nih.gov/pubmed/21841712>.
- [88] M. Thompson, “Reducing pressure ulcers in hip fracture patients.,” *British journal of nursing (Mark Allen Publishing)*, vol. 20, no. 15, 2011, ISSN: 0966-0461. [Online]. Available: <http://view.ncbi.nlm.nih.gov/pubmed/21841645>.
- [89] D. Carson, K. Emmons, W. Falone, and A. M. M. Preston, “Development of pressure ulcer program across a university health system.,” *Journal of nursing care quality*, Sep. 10, 2011, ISSN: 1550-5065. DOI: 10.1097/ncq.0b013e3182310f8b. [Online]. Available: <http://dx.doi.org/10.1097/ncq.0b013e3182310f8b>.

- [90] J. F. Greenleaf, M. Fatemi, and M. Insana, “Selected methods for imaging elastic properties of biological tissues.,” *Annual review of biomedical engineering*, vol. 5, no. 1, pp. 57–78, 2003, ISSN: 1523-9829. DOI: 10.1146/annurev.bioeng.5.040202.121623. [Online]. Available: <http://dx.doi.org/10.1146/annurev.bioeng.5.040202.121623>.
- [91] E. Brusseau, C. Perrey, P. Delachartre, M. Vogt, D. Vray, and H. Ernert, “Axial strain imaging using a local estimation of the scaling factor from RF ultrasound signals.,” *Ultrasonic imaging*, vol. 22, no. 2, pp. 95–107, Apr. 2000, ISSN: 0161-7346. [Online]. Available: <http://view.ncbi.nlm.nih.gov/pubmed/11061461>.
- [92] P. Hoskins, K. Martin, and A. Thrush, Eds., *Diagnostic Ultrasound Physics and Equipment*. Cambridge, UK: Cambridge University Press, 2010, ISBN: 978-0-521-75710-2.
- [93] T. U. S. National Library of Medicine, *Visible human project*, 1994.
- [94] J. C. Bamber and R. J. Dickinson, “Ultrasonic b-scanning: a computer simulation.,” *Physics in medicine and biology*, vol. 25, no. 3, pp. 463–479, May 1980, ISSN: 0031-9155. [Online]. Available: <http://view.ncbi.nlm.nih.gov/pubmed/7403261>.
- [95] T. A. Krouskop, T. M. Wheeler, F. Kallel, B. S. Garra, and T. Hall, “Elastic moduli of breast and prostate tissues under compression,” *Ultrasonic Imaging*, vol. 20, no. 4, pp. 260–274, Oct. 1, 1998, ISSN: 1096-0910. DOI: 10.1177/016173469802000403. [Online]. Available: <http://dx.doi.org/10.1177/016173469802000403>.
- [96] A. P. Choi and Y. P. Zheng, “Estimation of young’s modulus and poisson’s ratio of soft tissue from indentation using two different-sized indentors: finite element analysis of the finite deformation effect.,” *Med-*

- ical & biological engineering & computing*, vol. 43, no. 2, pp. 258–264, Mar. 2005, ISSN: 0140-0118. [Online]. Available: <http://view.ncbi.nlm.nih.gov/pubmed/15865137>.
- [97] A. D. Martin, M. Z. Daniel, D. T. Drinkwater, and J. P. Clarys, “Adipose tissue density, estimated adipose lipid fraction and whole body adiposity in male cadavers.,” *International journal of obesity and related metabolic disorders : journal of the International Association for the Study of Obesity*, vol. 18, no. 2, pp. 79–83, Feb. 1994, ISSN: 0307-0565. [Online]. Available: <http://view.ncbi.nlm.nih.gov/pubmed/8148928>.
- [98] J. Y. Rho, R. B. Ashman, and C. H. Turner, “Young’s modulus of trabecular and cortical bone material: ultrasonic and microtensile measurements.,” *Journal of biomechanics*, vol. 26, no. 2, pp. 111–119, Feb. 1993, ISSN: 0021-9290. [Online]. Available: <http://view.ncbi.nlm.nih.gov/pubmed/8429054>.
- [99] R. Shahar, P. Zaslansky, M. Barak, A. A. Friesem, J. D. Currey, and S. Weiner, “Anisotropic poisson’s ratio and compression modulus of cortical bone determined by speckle interferometry,” *Journal of Biomechanics*, vol. 40, no. 2, pp. 252–264, Jan. 2007, ISSN: 00219290. DOI: 10.1016/j.jbiomech.2006.01.021. [Online]. Available: <http://dx.doi.org/10.1016/j.jbiomech.2006.01.021>.
- [100] Y. Zheng, W. W. Lu, Q. Zhu, L. Qin, S. Zhong, and J. C. Leong, “Variation in bone mineral density of the sacrum in young adults and its significance for sacral fixation.,” *Spine*, vol. 25, no. 3, pp. 353–357, Feb. 1, 2000, ISSN: 0362-2436. [Online]. Available: <http://view.ncbi.nlm.nih.gov/pubmed/10703109>.

- [101] E. Brusseau, J. Kybic, J.-F. F. Deprez, and O. Basset, “2-D locally regularized tissue strain estimation from radio-frequency ultrasound images: theoretical developments and results on experimental data.,” *IEEE transactions on medical imaging*, vol. 27, no. 2, pp. 145–160, Feb. 2008, ISSN: 0278-0062. DOI: 10.1109/tmi.2007.897408. [Online]. Available: <http://dx.doi.org/10.1109/tmi.2007.897408>.
- [102] B. E. Treeby, J. Jaros, A. P. Rendell, and B. T. Cox, “Modeling non-linear ultrasound propagation in heterogeneous media with power law absorption using a k-space pseudospectral method.,” *The Journal of the Acoustical Society of America*, vol. 131, no. 6, pp. 4324–4336, Jun. 2012, ISSN: 1520-8524. DOI: 10.1121/1.4712021. [Online]. Available: <http://dx.doi.org/10.1121/1.4712021>.

Appendix A

Source Code

A.1 Quasi-Static Ultrasound Elastography Simulations

Listing A.1: convolvedBMode.m

```
1 function bmode = convolvedBMode(dbConnection, caseIndex, model)

3 % build our point spread function
query = [
5   'select waveSpeed, ...
6   'domainWidth, ...
7   'domainDepth, ...
8   'samplingFrequency, ...
9   'probingFrequency, ...
10  'numElements, ...
11  'numActiveElements, ...
12  'domainSeed, ...
13  'noiseMagnitude, ...
14  'Nx, ...
15  'Ny ...
```

```

    'from convBModes where id= ''' sprintf( '%d' , caseIndex ) '''  

    limit 1; ];  

17 results = fetch(dbConnection, query);  

19 waveSpeed = results.waveSpeed;  

samplingFrequency = results.samplingFrequency;  

21 depth = results.domainDepth;  

pointsPerM = samplingFrequency / waveSpeed;  

23 pointDepth = pointsPerM * depth;  

frequency = results.probingFrequency;  

25 wavelength = waveSpeed / frequency;  

pointsPerWaveLength = round(pointsPerM * wavelength);  

27 numElements = results.numElements;  

numActiveElements = results.numActiveElements;  

29 transducerWidth = results.domainWidth;  

windowWidth = numActiveElements * transducerWidth / numElements;  

31  

% interpolate our data for higher fidelity  

33 [xx, yy] = meshgrid(linspace(-results.domainWidth/2, results.  

domainWidth/2, results.Nx), linspace(0, depth, results.Ny));  

[ x, y ] = meshgrid(linspace(-results.domainWidth/2, results.  

domainWidth/2, numElements), linspace(0, depth, pointDepth));  

35  

% get our scatterer map  

37 rng(results.domainSeed);  

backgroundMap = 1 + results.noiseMagnitude * randn([ results.Ny,  

results.Nx]);  

39  

backgroundMap = interp2(xx, yy, backgroundMap, x, y, 'cubic');  

41 backgroundMap = (backgroundMap - min(min(backgroundMap)))/(max(  

max(backgroundMap)) - min(min(backgroundMap)));  

backgroundMap = 2*backgroundMap-1;  

43

```

```

% if we have a model input , deform our background map
45 if model ~= 0
    % extract our U and V from the model
47 [x, y, u, v] = extractUV([transducerWidth, depth], size(
backgroundMap), model);

49 % and store it in the db!
    saveMatrixInDB(dbConnection, 'convBModes', caseIndex, u, 'uMap
');
    saveMatrixInDB(dbConnection, 'convBModes', caseIndex, v, 'vMap
');

53 backgroundMap = compressBMode(x, y, backgroundMap, u, v);
end

55
% use a cos function to create the shape in the axial direction
57 xpsf = linspace(-windowWidth/2, windowHeight/2, 1*
pointsPerWaveLength);
    ypsf = linspace(0, 4*waveLength, 2*pointsPerWaveLength);
59 [xmpsf, ympsf] = meshgrid(xpsf, ypsf);
    psf = cos(2 * pi * frequency * ympsf / waveSpeed);

61
% lateral gaussian
63 mu = 0; sigma = windowHeight/4;
    gauss = (1 / (sigma * sqrt(2*pi))) * exp(-(xmpsf - mu).^2 / (2*
sigma.^2));
65 psf = psf .* gauss;

67
% axial gaussian
69 mu = 2*waveLength; sigma = waveLength*2;
    gauss = (1 / (sigma * sqrt(2*pi))) * exp(-(ympsf - mu).^2 / (2*
sigma.^2));

```

```

gauss = (gauss - min(min(gauss)))/(max(max(gauss)) - min(min(
gauss)));
71 psf = psf .* gauss;

73 % normalize it
psf = (psf - min(min(psf)))/(max(max(psf)) - min(min(psf)));
75 psf = 2*psf-1;

77 % now convolve!
bmode = conv2(backgroundMap, psf);

79 % and window it out
81 sz = size(bmode);
bmode = bmode(int32(floor((sz(1) - pointDepth) / 2)) : int32(
floor((sz(1) - pointDepth) / 2) + pointDepth - 1), int32(floor(
((sz(2) - numElements) / 2)) : int32(floor((sz(2) -
numElements) / 2) + numElements - 1));

83 % and post-process it
85 bmode = envelopeDetection(bmode)';
bmode = logCompression(bmode, 3, true);

87 % normalize it
89 bmode = (bmode - min(min(bmode))) ./ (max(max(bmode)) - min(min(
bmode)));
91 end

```

Listing A.2: compression.m

```

1 function model = compression(dbConnection, caseIndex)
% pull our data from our database
3 setdbprefs('DataReturnFormat', 'structure');

```

```

query = [...  

5      'select domainWidth , ...  

6      'domainDepth , ...  

7      'basalStiffness , ...  

8      'lesionStiffnessRatio , ...  

9      'density , ...  

10     'poissonsRatio , ...  

11     'caseCategory , ...  

12     'appliedStrain ...  

13     'from convBModes where id=' + sprintf( '%d' , caseIndex ) +'  

14     limit 1; ];  

parameters = fetch( dbConnection , query );  

15  

import com.comsol.model.*  

16  

import com.comsol.model.util.*  

17  

model = ModelUtil.create( 'Model' );  

18  

model.modelPath( 'compression' );  

19  

model.modelNode.create( 'mod1' );  

20  

model.geom.create( 'geom1' , 2 );  

21  

model.mesh.create( 'mesh1' , 'geom1' );  

22  

model.physics.create( 'solid' , 'SolidMechanics' , 'geom1' );  

23  

model.study.create( 'std1' );  

model.study( 'std1' ).feature.create( 'stat' , 'Stationary' );  

model.study( 'std1' ).feature( 'stat' ).activate( 'solid' , true );

```

```

35 model.param.set('modelWidth', sprintf('%f [m]', parameters.
domainWidth));
36 model.param.set('modelDepth', sprintf('%f [m]', parameters.
domainDepth));
37 model.param.set('appliedStrain', sprintf('%f', parameters.
appliedStrain));
38 model.param.set('compression', 'modelDepth*appliedStrain');
39 model.param.set('basalStiffness', sprintf('%f [Pa]', parameters.
basalStiffness));
40 model.param.set('stiffnessRatio', sprintf('%f', parameters.
lesionStiffnessRatio));
41 model.param.set('lesionStiffness', 'basalStiffness*'
stiffnessRatio');
42 model.param.set('lesionExtraStiffness', 'lesionStiffness -'
basalStiffness');
43 model.param.set('density', sprintf('%f [kg/m^3]', parameters.
density));
44 model.param.set('poissonsRatio', sprintf('%f', parameters.
poissonsRatio));
45
46 % deal with the human model case
47 if strcmpi(cell2mat(parameters.caseCategory), 'human') == 1
48 model.param.set('fatStiffness', '80[kPa]');
49 model.param.set('boneStiffness', '18.6[GPa]');
50 model.param.set('fatExtraStiffness', 'fatStiffness -'
basalStiffness');
51 model.param.set('boneExtraStiffness', 'boneStiffness -'
basalStiffness');

52
53 % import our stiffness image
54 model.func.create('im1', 'Image');
55 model.func('im1').set('filename', sprintf('/media/kenton/data/
School/USEbrella/Programs/QuasiRedo/compression/stiffnessMap_')

```

```

%03d.png', caseIndex));

model.func('im1').importData;

model.func('im1').set('xmin', sprintf('%f', (-parameters.
domainWidth / 2)));

model.func('im1').set('xmax', sprintf('%f', (parameters.
domainWidth / 2)));

model.func('im1').set('ymax', sprintf('%f', parameters.
domainDepth));

model.func('im1').set('inplace', 'off');

model.func('im1').set('scaling', 'manual');

model.func('im1').set('manualexpr', 'r');

model.func('im1').set('funcname', 'lesionMap');

model.func.duplicate('im2', 'im1');

model.func('im2').set('funcname', 'boneMap');

model.func('im2').set('manualexpr', 'b');

model.func.duplicate('im3', 'im2');

model.func('im3').set('funcname', 'fatMap');

model.func('im3').set('manualexpr', 'g');

else

% import our stiffness image

model.func.create('im1', 'Image');

model.func('im1').set('funcname', 'stiffnessMap');

model.func('im1').set('filename', sprintf('/media/kenton/data/
School/USErella/Programs/QuasiRedo/compression/stiffnessMap_.

%03d.png', caseIndex));

model.func('im1').importData;

model.func('im1').set('xmin', sprintf('%f', (-parameters.
domainWidth / 2)));

model.func('im1').set('xmax', sprintf('%f', (parameters.
domainWidth / 2)));

model.func('im1').set('ymax', sprintf('%f', parameters.
domainDepth));

%model.func('im1').set('flipy', true);

```

```

    end

81
model.geom( 'geom1' ).feature.create( 'r1' , 'Rectangle' );
83 model.geom( 'geom1' ).feature( 'r1' ).setIndex( 'size' , 'domainWidth'
, 0 );
model.geom( 'geom1' ).feature( 'r1' ).setIndex( 'size' , 'domainDepth'
, 1 );
85 model.geom( 'geom1' ).feature( 'r1' ).setIndex( 'size' , 'modelWidth' ,
0 );
model.geom( 'geom1' ).feature( 'r1' ).setIndex( 'size' , 'modelDepth' ,
1 );
87 model.geom( 'geom1' ).feature( 'r1' ).setIndex( 'pos' , '-modelWidth/2'
, 0 );
model.geom( 'geom1' ).run;

89
model.physics( 'solid' ).feature( 'lemm1' ).set(
90     'NearlyIncompressible' , 1 , '1' );
model.physics( 'solid' ).feature( 'lemm1' ).set( 'E_mat' , 1 , 'userdef'
);
% deal with the human model case
93 if strcmpi( cell2mat( parameters.caseCategory ) , 'human' ) == 1
    model.physics( 'solid' ).feature( 'lemm1' ).set( 'E' , 1 , '
basalStiffness + (fatMap(x, modelDepth - y) *
fatExtraStiffness) + (lesionMap(x, modelDepth - y) *
lesionExtraStiffness) + (boneMap(x, modelDepth - y) *
boneExtraStiffness)' );
95 else
    model.physics( 'solid' ).feature( 'lemm1' ).set( 'E' , 1 , '
basalStiffness+(stiffnessMap(x,modelDepth-y)*
lesionExtraStiffness)' );
end
97 model.physics( 'solid' ).feature( 'lemm1' ).set( 'nu_mat' , 1 , 'userdef' );

```

```

99 model.physics('solid').feature('lemm1').set('nu', 1, '
  poisonsRatio');

model.physics('solid').feature('lemm1').set('rho_mat', 1, '
  userdef');

101 model.physics('solid').feature('lemm1').set('rho', 1, 'density')
  ;

model.physics('solid').feature.create('fix1', 'Fixed', 1);

103 model.physics('solid').feature('fix1').selection.set([2]);

model.physics('solid').feature.create('disp1', 'Displacement1',
  1);

105 model.physics('solid').feature('disp1').selection.set([3]);

model.physics('solid').feature('disp1').set('Direction', 2, '1')
  ;

107 model.physics('solid').feature('disp1').set('U0', 2, '-'
  compression);

109 model.mesh('mesh1').feature.create('ftri1', 'FreeTri');

model.mesh('mesh1').feature('size').set('hauto', '1');

111 model.mesh('mesh1').run;

113 model.sol.create('sol1');

model.sol('sol1').study('std1');

115 model.sol('sol1').feature.create('st1', 'StudyStep');

model.sol('sol1').feature('st1').set('study', 'std1');

117 model.sol('sol1').feature('st1').set('studystep', 'stat');

model.sol('sol1').feature.create('v1', 'Variables');

119 model.sol('sol1').feature('v1').set('control', 'stat');

model.sol('sol1').feature.create('s1', 'Stationary');

121 model.sol('sol1').feature('s1').feature.create('fc1', '
  FullyCoupled');

model.sol('sol1').feature('s1').feature.remove('fcDef');

123 model.sol('sol1').attach('std1');

```

```

125     model.sol('sol1').runAll;
end

```

Listing A.3: StrainImage.m

```

function [alpha, tau] = StrainImage( I1, I2, L, deltaAx, maxX,
    numPoints, columnRadius, maxAlpha )

2
columns = size(I1, 2);

4
alpha = zeros(maxX / deltaAx, columns);
tau = zeros(maxX / deltaAx, columns);
h = 0;

8
tStart = tic;

10
parfor-progress(columns);
parfor i = 1:columns
    [alpha(:, i), tau(:, i)] = Strain(I1(:, i), I2, L, deltaAx
        , maxX, numPoints, h, i, columns, columnRadius, maxAlpha);
    parfor-progress;
end
parfor-progress(0);

18
processingTime = toc(tStart);
fprintf('Elastogram took %s!\n', datestr(processingTime / 3600
    / 24, 'HH:MM:SS'));
20
end

```

Listing A.4: Strain.m

```

1 function [alpha, tau] = Strain( I1, I2, L, deltaAx, maxX,
    numPoints, h, column, columns, columnRadius, maxAlpha )

```

```

3      M = maxX / deltaAx ;
4      alpha = [] ;
5      tau = [] ;
6
7      for m = 1:M
8          pr1 = Pr1(m, deltaAx) ;
9          pr2 = Pr2(alpha , deltaAx) ;
10
11         r1 = R1( I1 , pr1 , L, numPoints ) ;
12         alphas = maxAlpha:-0.001:1;
13         taus = zeros( size(alphas)) ;
14         correlations = zeros( size(alphas)) ;
15
16         for i = 1:length(alphas)
17             columnCorrelations = [] ;
18             for c = (column-columnRadius):(column+columnRadius)
19                 % make sure we have a valid column
20                 if (c < 1) || (c > columns)
21                     continue ;
22                 end
23
24                 % get the part of the image we need
25                 r2 = R2( I2(:, c) , pr2 , L / alphas(i) , numPoints )
26                 ;
27
28                 % and correlate it
29                 columnCorrelations = [columnCorrelations ,
30                 Correlate(r1 , r2)] ;
31
32             end
33
34             % now pick the best column that had the lowest
35             correlation for

```

```

% this alpha
33    c = -columnRadius : column+columnRadius ;
        [ correlations( i ) , mindex ] = min(columnCorrelations) ;
35    taus( i ) = c(mindex) ;
end
37
% only use the estimated alpha if the slope isn't too
steep
39    [ ~ , mindex ] = min(correlations) ;
40    if m > (M/3)
41        if abs(alphas(mindex) - alpha(length(alpha))) > 0.02
42            alpha = [ alpha ; alpha(length(alpha)) ] ;
43            tau = [ tau ; tau(length(tau)) ] ;
44        else
45            alpha = [ alpha ; alphas(mindex) ] ;
46            tau = [ tau ; taus(mindex) ] ;
47        end
48    else
49        alpha = [ alpha ; alphas(mindex) ] ;
50        tau = [ tau ; taus(mindex) ] ;
51    end
52
53 end
54
55 end

```